SNAP25 disease mutations change the energy landscape for synaptic exocytosis due to aberrant SNARE interactions

Anna Kádková[1,3], Jacqueline Murach[2,3], Maiken Ø. Pedersen[1,3], Andrea Malsam[2], Jörg Malsam[2], Thomas H. Söllner[2], and Jakob B. Sørensen[1]

[1] Department of Neuroscience, University of Copenhagen, Blegdamsvej 3B, 2200 Copenhagen N, Denmark.

[2] Heidelberg University Biochemistry Center, 69120 Heidelberg, Germany.

[3]These authors contributed equally.

Running title: SNAP25 disease mutations changing priming and energy barriers

*Correspondence to:

Jakob B. Sørensen
Department of Neuroscience
University of Copenhagen
Blegdamsvej 3B
2200 Copenhagen N
Denmark.
Email: jakobbs@sund.ku.dk.

Abstract

SNAP25 is one of three neuronal SNAREs driving synaptic vesicle exocytosis. We studied three mutations in SNAP25 that cause epileptic encephalopathy: V48F, and D166Y in the Synaptotagmin-1 (Syt1) binding interface, and I67N, which destabilizes the SNARE-complex. All three mutations reduced Syt1-dependent vesicle docking to SNARE-carrying liposomes and Ca^{2+}-stimulated membrane fusion *in vitro* and in neurons. The V48F and D166Y mutants (with potency D166Y > V48F) led to reduced Readily Releasable Pool (RRP) size, due to increased spontaneous (mEPSC) release and decreased priming rates. These mutations lowered the energy barrier for fusion and increased the release probability, which are gain-of-function features not found in *Syt1* knockout (KO) neurons; normalized mEPSC release rates were higher (potency D166Y>V48F) than in the *Syt1* KO. These mutations (potency D166Y > V48F) increased spontaneous association to partner SNAREs, resulting in unregulated membrane fusion. In contrast, the I67N mutant decreased mEPSC frequency and EPSC amplitudes due to an increase in the apparent height of the energy barrier for fusion, whereas the RRP size was unaffected. This could be partly compensated by positive charges lowering the energy barrier. Overall, pathogenic mutations in SNAP25 cause complex changes in the energy landscape for priming and fusion.

41 ## Introduction

42 The fusion machinery responsible for chemical synaptic transmission is well known: it consists of
43 the SNARE-complex, a ternary complex formed by the proteins VAMP2, syntaxin-1 and SNAP25
44 (Sutton et al., 1998). This complex is under tight control by upstream partner protein Munc18-1,
45 which acts as a template for SNARE-complex formation, and Munc13s, which assist in the transitions
46 required along the pathway of assembly (Rizo, 2022). SNARE-complexes assemble in a zipper-like
47 manner; partially assembled SNAREpins bind synaptotagmin-1 (Syt1) and complexin within two
48 separate interaction sites: the primary interface formed between a synaptotagmin 1 molecule and
49 syntaxin-1 and SNAP25 (Zhou et al., 2015), and the tripartite interface formed by syntaxin-1 and
50 VAMP2 with another Syt1 molecule and complexin (Zhou et al., 2017). Upon arrival of an action
51 potential, Ca^{2+} binds to the two C2-domains of Syt1, which results in rapid vesicle-plasma membrane
52 fusion and release of neurotransmitter within a fraction of a millisecond (Sudhof, 2013).

53 The strong functional integration and specialization of the neuronal SNARE for speed has rendered
54 the release machinery exquisitely susceptible to insults. *De novo* mutations in SNAREs and
55 associated proteins lead to complex neurological disease, characterized by drug-resistant epilepsy,
56 intellectual disability, movement disorders and often autism; a syndrome which has been denoted
57 "SNAREopathy" (Verhage and Sorensen, 2020). Although rare, these are devastating conditions for
58 the patients and their families. Consequently, there is considerable interest in revealing the
59 molecular/cellular mechanisms for these conditions, which is seen as key to the development of
60 treatment. Disease-causing mutations in the SNARE-machinery fall into distinct categories according
61 to the nature of the defect (Verhage and Sorensen, 2020). These include different forms of haplo-
62 insufficiency, where the mutated protein is either lost altogether or has lost its functionality, and
63 dominant-negative or recessive variants, as well as variants with new or changed protein
64 interactions, referred to as neomorphs.

65 Most disease mutations have been described in *STXBP1* (Abramov et al., 2021a; Verhage and
66 Sorensen, 2020; Xian et al., 2022), the gene encoding Munc18-1. These mutations are generally
67 found to cause Munc18-1 hypo-expression and thus the mutations belong in the haploinsufficiency
68 category. In some cases, associated synaptic phenotypes have been identified, often a decrease in
69 evoked release (Kovacevic et al., 2018); however, for other mutants no electrophysiological

correlate was found (Kovacevic et al., 2018). The reason for haploinsufficiency/hypoexpression of most *STXBP1* disease mutations has been suggested to be protein instability, leading to degradation (Guiberson et al., 2018; Kovacevic et al., 2018; Martin et al., 2014; Saitsu et al., 2008). Consequently, attempts to rescue the disease phenotypes have focused on mechanisms for increasing general expression levels, for instance chemical chaperones that might prevent Munc18-1 misfolding and degradation (Abramov et al., 2021b; Guiberson et al., 2018).

The situation is different for disease mutations in Syt1 and SNAP25. In these cases, mutation generally does not cause protein instability, but instead changes function in different ways. For Syt1, disease mutations were found to cluster in the C2B-domain around the top loops that coordinate Ca^{2+} (Baker et al., 2018). Expression of these mutants in neurons demonstrated reduced evoked release, in some cases an increase in spontaneous release, and a dominant-negative phenotype when co-expressed with wildtype protein (Bradberry et al., 2020). The molecular mechanism was identified as a decrease in Ca^{2+}-dependent lipid binding (Bradberry et al., 2020). In SNAP25, disease causing mutations are found within the SNARE-domains (Hamdan et al., 2017; Klockner et al., 2021; Rohena et al., 2013; Shen et al., 2014). Alten et al. studied a selection of SNAP25 mutants, and found no changes in expression levels, but changes in both spontaneous and evoked release (Alten et al., 2021). Specifically, mutations in the primary Syt1:SNARE interface (Zhou et al., 2015) caused an increase in spontaneous release rates, and a decrease in evoked release amplitudes. Conversely, C-terminal mutations in the so-called ‘layer residues’, whose side chains point to the center of the SNARE complex and are involved in SNAREpin zippering (Sutton et al., 1998), led to a decrease in both evoked and spontaneous release (Alten et al., 2021). This is expected because the C-terminal end of the SNARE-complex is required for both types of release (Weber et al., 2010).

Alten et al. (2021) described striking phenotypes for most SNAP25 mutations tested, but the molecular reason for these phenotypes remains incompletely understood, and a few findings were surprising. For instance, Alten et al. reported that the V48F and D166Y mutants supported an unchanged Readily Releasable Pool (RRP) of vesicles. The RRP is the pool of vesicles available for immediate release upon invasion of the presynapse by the action potential, and it is often assessed by applying a hyperosmotic solution (often 0.5 M sucrose), which causes primed vesicles to fuse (Rosenmund and Stevens, 1996). Previously, we concluded that the primary Syt1:SNARE-interface is involved in vesicle priming (Schupp et al., 2016), which agrees with the suggestion that Syt1 binds

100 to the SNAREs before Ca^{2+} arrival (Zhou et al., 2015). Conversely, Alten et al. reported a smaller RRP
101 for the I67N mutant, but the I67 residue is present in the internal of layer +4, which we expected to
102 affect final SNARE complex zippering causing membrane fusion rather than priming (Sorensen et al.,
103 2006; Weber et al., 2010). Another open question is whether the phenotype of the mutants in the
104 primary interface (V48F, D166Y) are explainable solely by the loss of Syt1 binding, or whether other
105 features of these mutations add to, or detract from, the phenotype.

106 Here, we reexamined three SNAP25 disease mutations: I67N, V48F and D166Y. We confirmed the
107 increase in spontaneous release rate and decrease in evoked release by V48F and D166Y reported
108 previously (Alten et al., 2021). Through *in vitro* analysis we find that both mutations lower Syt1
109 association to SNARE-protein liposomes. Additional experiments both *in vitro* and in cells
110 demonstrate that V48F and especially D166Y represent partial gain-of-function mutations that
111 increase association to partner SNAREs and lower the energy barrier for fusion, bypassing Syt1-
112 dependent control. Thus, these mutants do not phenocopy the loss of Syt1, but combine loss of Syt1
113 binding with a gain-of-function phenotype. At the same time, the mutants act as loss-of-function in
114 upstream reactions, through effects on priming. The I67N is a classical dominant-negative mutation,
115 which increases the energy barrier for fusion, but does not change the size of the RRP if probed by
116 a sufficiently high concentration of sucrose, nor does the I67N change the electrostatics of triggering
117 itself. Thus, for V48F and D166Y, loss-of-function and gain-of-function features combine to change
118 the energy landscape for vesicle priming and fusion in a complex way. These findings have
119 consequences for our understanding of the simultaneous role of the primary SNARE:Syt1 interface
120 in vesicle priming and release clamping. It further demonstrates the challenge faced by finding
121 mechanism-based treatments of these disorders in the presence of multiple effects caused by single
122 point mutations.

123 **Results**

124 We first investigated two SNAP25 disease-causing mutations within the primary Syt1:SNARE-
125 interface (V48F, D166Y; Fig. 1A-C). The mutations occurred *de novo* and were identified in single
126 heterozygous subjects. The V48F mutant was identified in a 15-year-old female with
127 encephalopathy, intellectual disability and generalized epilepsy with seizures started at 5 months of
128 age; MRI was normal except for delayed myelination (Rohena et al., 2013). The D166Y mutants was
129 found in a 23-year-old male with global developmental delay, nocturnal tonic-clonic seizures, and
130 moderate intellectual disability; the MRI showed mild diffuse cortical atrophy (Hamdan et al., 2017).
131 We aimed to achieve a detailed understanding of the reason for synaptic dysfunction.

132 *The V48F and D166Y mutants disinhibit spontaneous release and desynchronize evoked release*

133 We constructed lentiviral vectors, which expressed wildtype (WT) or mutant SNAP25b fused N-
134 terminally to EGFP as an expression marker (Delgado-Martinez et al., 2007). In the absence of
135 SNAP25, neuronal viability is compromised (Delgado-Martinez et al., 2007; Peng et al., 2013; Santos
136 et al., 2017; Weber et al., 2010) with low-density autaptic glutamatergic neurons dying within a few
137 days, whereas *Snap25* KO neurons growing at higher densities, or in the intact brain, can survive
138 longer, but also eventually degenerate (Bronk et al., 2007; Hoerder-Suabedissen et al., 2019). We
139 therefore first examined the morphology and survival of autaptic hippocampal neurons from
140 *Snap25* KO after expressing mutated or WT EGFP-SNAP25b (henceforth denoted 'WT' in rescue
141 experiments; not to be confused with '*Syt1* WT', which refers to wildtype littermates of *Syt1* KO
142 mice).

143 As expected, *Snap25* KO autaptic neurons did not survive in the absence of expression of
144 exogeneous SNAP25 (Fig. 2E), whereas expression of WT EGFP-SNAP25b restored survival (Delgado-
145 Martinez et al., 2007; Ruiter et al., 2019; Weber et al., 2010). Both mutations (V48F and D166Y)
146 caused rescue of survival; however, the number of neurons per islet was lower than in WT-
147 expressing neurons prepared in parallel. This difference was statistically significant for D166Y, but
148 not for V48F (Fig. 2E). Since patients harbor one mutated and one WT allele, we coexpressed WT
149 EGFP-SNAP25b with mutated EGFP-SNAP25b, by combining infection with separate viruses
150 encoding WT and mutant protein in a 1:1 ratio, as done previously by others for Syt1 (Bradberry et
151 al., 2020). As a prerequisite for this, we demonstrated by Western blot analysis that all mutant

152 viruses expressed similar amounts of protein as WT viruses (Fig. 2A). In co-expressing neurons, we
153 added half the volume of WT and mutant virus as compared to the WT condition, thus keeping the
154 total amount of virus constant. We preferred to combine two single-cistronic viruses, rather than to
155 construct bicistronic viruses, since the larger insert would be expected to lower the titer of viruses,
156 which might compromise survival rescue of *Snap25* KO neurons. Using co-expression of WT and
157 mutant SNAP25b, neuronal survival was mildly and significantly reduced in the V48F + WT condition
158 from WT (Fig. 2E). Overall, mutations seemed to mildly reduce survivability of neurons. Staining of
159 neurons against VGlut1 (a marker for glutamatergic synapses) and MAP2 (a dendritic marker)
160 revealed no significant difference in the dendritic length or the number of synapses in neurons
161 expressing V48F, and D166Y alone (Fig. 2B-D).

162 Patch-clamp was performed on days 10-14 on autaptic neurons expressing either the WT EGFP-
163 SNAP25b, the mutants, or both the mutant and WT in a 1:1 ratio. Spontaneous miniature events
164 were recorded at a holding voltage of -70 mV. Both primary interface mutations (V48F, D166Y)
165 strongly increased the frequency of mEPSCs (Fig. 3A-B, D-E); the mEPSC amplitude was significantly
166 increased in the V48F, and insignificantly (p=0.14) increased for the D166Y (Fig. 3C, F). The mEPSC
167 frequency was at least as high as in *Syt1* KO neurons measured in separate experiments (Fig. 3G-I).
168 V48F and D166Y co-expressed with WT resulted in mEPSC frequencies close to the arithmetic mean
169 between frequencies in WT and the mutant alone (Fig. 3B, E), indicating that the mutations are
170 incompletely dominant, or co-dominant.

171 Brief depolarization elicits an unclamped action potential in the axon, which makes it possible to
172 study evoked release, which is essentially absent in *Snap25* KO neurons (Bronk et al., 2007; Delgado-
173 Martinez et al., 2007). The V48F and D166Y mutants both supported evoked release, but the evoked
174 EPSC (eEPSC) amplitude was significantly reduced in the mutant condition (Fig. 4A-B, E-F), whereas
175 when co-expressed with the WT, only the D166Y mutant had a significantly reduced EPSC (Fig. 4B,F).
176 Integration of individual eEPSCs allowed determination of the total charge and the assessment of
177 synchronous and asynchronous release components (Fig. 4 – Figure supplement 1). The eEPSC
178 charge was significantly reduced in the D166Y, but not in the V48F (Fig. 4C,G), whereas in both cases
179 the kinetics was significantly shifted in the direction of more asynchronous release, and the fast
180 time constant was prolonged (Fig. 4D,H; Fig. 4 - Figure supplement 2). We compared the data
181 obtained from V48F and D166Y SNAP25 to *Syt1* KO neurons recorded in separate experiments. *Syt1*

182 WT neurons in this set of experiments had larger EPSC amplitudes, and a larger charge than WT-
183 rescued *Snap25* KO neurons (Fig. 4I,J,K), which might be caused by differences between cell cultures,
184 or animal lines (*SNAP25* vs *Syt1* lines). Note that our experiments using WT, mutant and WT +
185 mutant SNAP25 was always carried out in neurons prepared and recorded in parallel from the same
186 SNAP25 KO embryos (Materials and Methods). In the *Syt1* KO, the kinetic change was similar to the
187 V48F and D166Y (Fig. 4L), but the total charge was also strongly reduced (Fig. 4K), unlike the two
188 mutations that displayed at most a mild reduction (Fig. 4C,G).

189 Overall, D166Y and V48F caused a strong disinhibition of spontaneous release and a
190 desynchronization of evoked release, as demonstrated before (Alten et al., 2021), and consistent
191 with previous mutational studies of the primary interface, both in SNAP25 (Schupp et al., 2016) and
192 Syt1 (Zhou et al., 2015). Accordingly, these phenotypes are similar to *Syt1* KO, but the effect of V48F
193 and D166Y on total evoked charge was milder than in the *Syt1* KO. The preserved overall charge of
194 evoked release in V48F and mild reduction in D166Y might point to a compensatory gain-of-function
195 aspect to these mutations, in addition to the impaired Syt1 interaction.

196 *V48F and D166Y mutations lower the energy barrier for release and reduce the readily releasable*
197 *pool size*

198 The role of Syt1 and Syt1:SNARE interactions in vesicle priming has been controversially discussed.
199 The RRP is often assessed by applying a pulse of hypertonic solution to the neurons, usually 0.5 M
200 sucrose (Rosenmund and Stevens, 1996; Schotten et al., 2015). However, in some experiments this
201 did not lead to a change in RRP size in the absence of Syt1 (Bacaj et al., 2015; Xu et al., 2009),
202 whereas experiments both from our laboratories and others showed a decrease in RRP in the
203 absence of Syt1 (Bouazza-Arostegui et al., 2022; Chang et al., 2018; Courtney et al., 2019; Huson et
204 al., 2020; Liu et al., 2009; Ruiter et al., 2019). The reason for this discrepancy is likely partly technical
205 and has to do with how fast sucrose can be applied to the dendritic tree (see also Discussion). Using
206 neurons growing on small autaptic islands makes it possible to apply sucrose to the entire dendritic
207 tree (which is confined to the 30-50 µm island) within tens of milliseconds, which is fast enough to
208 dissect the RRP with a short (few s) sucrose application. We set out to understand whether the V48F
209 and D166Y mutants changed the size of the RRP.

210 Application of 0.5M sucrose to neurons with the V48F or D166Y mutation resulted in estimates of
211 the RRP (denoted $RRP_{0.5}$) that were significantly reduced compared to the WT condition (Fig. 5
212 A,C,F,H). Also the co-expressed condition displayed significantly reduced $RRP_{0.5}$. Application of two
213 different sucrose concentrations is used to probe the size of the energy barrier for release (Basu et
214 al., 2007; Schotten et al., 2015), because the use of a lower sucrose concentration (typically 0.25 M)
215 will only release a fraction of the RRP, and this fraction depends sensitively on the energy barrier
216 for release; the size of the RRP at 0.5M sucrose ($RRP_{0.5}$) is used for normalization. Application of 0.25
217 M sucrose to V48F and D166Y expressing neurons strikingly led to unchanged pool release ($RRP_{0.25}$)
218 (Fig. 5B,G). Consequently, the ratio of pools ($RRP_{0.25}/RRP_{0.5}$) was significantly increased for both the
219 V48F and the D166Y mutations (Fig. 5D,I), indicating that these two mutations decrease the
220 apparent energy barrier for fusion (Schotten et al., 2015). The co-expressed conditions were in-
221 between WT and mutant and did not reach statistical significance. Consistent with these results,
222 both mutations on average increased the release probability, calculated as the ratio between the
223 eEPSC charge and the $RRP_{0.5}$ charge measured in the same cell. The increase was statistically
224 significant for the D166Y mutation (Fig. 5J), but not for V48F (Fig. 5E). This is different from the
225 situation in the *Syt1* KO, where the $RRP_{0.25}/RRP_{0.5}$ and the release probability were both significantly
226 decreased (Fig. 5K-O), although in this data set the reducint in $RRP_{0.5}$ size by by removing Syt1 did
227 not reach statistical significance (P=0.0548, unpaired t-test). Thus, the increased mEPSC release rate
228 from the *Syt1* KO does not correlate with a reduced energy barrier as assayed by sucrose, which was
229 reported before (Huson et al., 2020), and the V48F and D166Y have specific gain-of-function
230 features that lower the energy barrier for vesicle fusion.

231 To investigate the reasons for the change in RRP-size by D166Y and V48F, we considered a one-pool
232 model for the RRP (Fig. 6A), where the RRP is filled by priming (k_1) from an upstream pool and
233 depleted by de-priming (k_{-1}) or fusion (k_f). Dividing the miniature release rates (r_{mini}) with the size of
234 the RRP yields the spontaneous fusion rate k_f. The current plateau during 0.5 M sucrose application
235 (Fig. 6B) essentially reports on the priming rate (k_1), providing that the fusion rate is sufficiently
236 increased by sucrose (Materials and Methods). However, high sucrose concentrations can change
237 the baseline current level, which will cause an error in estimation of k_1. We therefore corrected the
238 plateau level using a plot of the variance versus mean during the sucrose application (Fig. 6C); this
239 plot is linear for the type of noise generated by synaptic transmission (shot noise). Back-

240 extrapolation of a regression line allows a determination of the baseline current level in the
241 presence of sucrose (Fig. 6B-C; see Materials and Methods). Combining RRP size with the estimates
242 of k_1 and k_f allows determining the depriming rate, k_{-1}.

243 These calculations showed that k_f, the spontaneous fusion rate was strongly increased in the V48F
244 and D166Y, and this increase was much larger for the mutations than for the *Syt1* KO (Fig. 6D)
245 fulfilling D166Y>V48F>*Syt1* KO. Further analysis showed that in both mutations, the forward priming
246 rate, k_1, and the depriming rate, k_{-1}, were both decreased – the latter effect was only significant for
247 D166Y (Table 1). Summing up the effects of changes in the three parameters on the RRP-size for the
248 V48F, D166Y and *Syt1* KO (Fig. 6E), we can conclude that for the V48F and even more for the D166Y,
249 spontaneous release contributes to the reduction in RRP size, whereas this effect is minimal in the
250 *Syt1* KO. However, the major reason for the smaller RRP size is a reduction in priming rate, k_1, which
251 is partly counteracted by the decrease in k_{-1} (which would increase RRP size). Overall, changes in
252 priming, depriming and spontaneous fusion rates combine to change RRP size.

253 Repetitive stimulation to determine the RRPs often results in lower estimates than sucrose
254 application, because action potentials draw on a sub-pool of the RRP (Moulder and Mennerick,
255 2005), whereas sucrose releases the entire RRP (Rosenmund and Stevens, 1996). To determine the
256 RRP sub-pool that evoked release draws on (denoted RRP_{ev}) we applied repetitive stimulation (50
257 APs @ 40 Hz) and used back-extrapolation to determine the RRP (Neher, 2015). Performing this in
258 our standard 2 mM Ca^{2+}-containing extracellular solution resulted in overall smaller estimates for
259 RRP_{ev} for V48F and D166Y compared to WT (Fig. 7 - Figure supplement 1); however, the differences
260 were not statistically significant. The back-extrapolation method works best with high release
261 probabilities (Neher, 2015); therefore, we repeated these experiments in the presence of 4 mM
262 extracellular Ca^{2+}. Under these conditions, the RRP_{ev} was significantly reduced for both the V48F
263 and D166Y mutation (Fig. 7C,G; Fig. 7 - Figure supplement 2). Strikingly, the release probabilities
264 (calculated as the charge of the first EPSC of the train divided by the RRP_{ev}) were decreased for both
265 mutations (Fig. 7D,H), which correlated with an increased paired-pulse ratio (Fig. 7A,E, *inserts)*
266 (Zucker and Regehr, 2002). Thus, although the release probability calculated by normalizing evoked
267 charge to the sucrose-determined RRP ($RRP_{0.5}$) was increased (see above), the release probability
268 when normalizing to RRP_{ev} was decreased. This points to a difference in the organization of the
269 RRP_{ev} and $RRP_{0.5}$ (see Discussion). The forward priming rate is determined as the slope of the linear

270 fit used for the back extrapolation; this parameter was reduced in both mutations (Fig. 7B, F; Fig. 7
271 - Figure supplement 2). Thus, the difference in priming rate extends to the RRP_{ev}.

272 Overall, these data demonstrate a rather complex phenotype of the D166Y and V48F mutations,
273 which combine a lowering of the energy barrier – a gain-of-function feature – with a loss of vesicle
274 priming – a loss-of-function feature. The D166Y and V48F phenotypes can be summarized as 1)
275 desynchronized EPSCs with at most mildly reduced total charge, 2) lowered energy barrier for
276 fusion, 3) increased release probability when normalized to the sucrose pools, 4) decreased RRP-
277 size due to unclamped spontaneous release and lowered forward priming rates, 5) short-term
278 facilitation. These phenotypes are distinctive from the Syt1 KO, which does not have a preserved
279 charge of the EPSC, or lowered energy barrier when probed by sucrose, or an increased release
280 probability. Thus, the D166Y and V48F cannot be understood solely in terms of a lack of Syt1
281 coupling; instead, gain-of-function features are present in the mutants which are absent upon
282 deletion of Syt1.

283 *V48F and D166Y mutants show increased partner SNARE interactions and cause unregulated fusion*
284 *in vitro*

285 We next tried to identify the biochemical properties of V48F and D166Y, which could support a gain-
286 of-function phenotype during exocytosis. These data are displayed in Fig. 8-9 - data on the I67N
287 mutant were obtained in parallel and will be presented later. To test to which degree the mutants
288 may change the stability of SNARE complexes, full-length t-SNAREs (syntaxin-1 and SNAP25) were
289 incubated with the cytosolic domain of VAMP2 (VAMP2cd) overnight. Cis-SNARE complex stability
290 was tested in the presence of SDS at the indicated temperatures (Fig. 8A), and the release of
291 syntaxin-1 as a single protein band was used as a measure of the complex dissociation. The wildtype
292 (WT), V48F and D166Y v-/t-SNARE complexes showed a similar stability with half-maximal
293 dissociation occurring at approximately 71°C.

294 Next, we asked whether the V48F and D166Y mutants would change interaction with Syt1. To this
295 end, Atto647 labelled Giant Unilamellar Vesicles (GUVs) filled with isosmotic sucrose and containing
296 preassembled t-SNARE complexes were preincubated with Atto488/Atto550 labeled Small
297 Unilamellar Vesicles (SUVs) containing Syt1 as well as VAMP2 for 10 minutes on ice, followed by
298 centrifugation to reisolate GUVs with attached SUVs. Fusion was blocked by performing the assay

299 on ice. Attachment of SUVs was determined by measuring the Atto550 fluorescence of SUVs. In the
300 absence of PI(4,5)P_2, vesicle attachment occurs by Syt1:SNARE interactions (Kim et al., 2012;
301 Parisotto et al., 2012), probably involving the primary interface (Zhou et al., 2015). In the cell,
302 PI(4,5)P_2-binding by Syt1 appears to happen first (Honigmann et al., 2013), whereas subsequent
303 Syt1:SNARE-binding leads to a tightly docked state (Chen et al., 2021). Under our conditions, both
304 SNAP25 mutants (V48F and D166Y) showed significantly impaired attachment of Syt1/VAMP2 SUVs
305 to t-SNARE GUVs (Fig. 8B). Both V48 and D166 directly interact with Syt1 (Fig. 1B-C, (Zhou et al.,
306 2015)), so that changing these two amino acids to more bulky or hydrophobic amino acids reduced
307 the docking from 42.7 ± 2.6 % wildtype (WT) docking efficiency to 29.6 ± 4.1 % and 20.9 ± 3.7 %,
308 respectively. In the presence of 1% PI(4,5)P_2, the vesicle attachment increased from 42.7 ± 2.6 % to
309 66.0 ± 0.5 % for WT t-SNARE. Although the Syt1:PI(4,5)P_2 interaction predominated SUV-GUV
310 docking, both mutants still showed significantly reduced vesicle attachment by approximately 6%
311 compared to WT (Fig. 8C) (V48F: 59.1 ± 1.4 %, and D166Y: 60.0 ± 2.0 %).

312 To understand how the mutations affect fusion in a well-defined reconstituted membrane fusion
313 system, we performed *in vitro* lipid mixing assays using GUVs containing both t-SNAREs (syntaxin-1
314 and SNAP25) with 1% PI(4,5)P_2, and 0.5% Atto488/0.5% Atto550 labeled SUVs containing Syt1 and
315 VAMP2 in the presence or absence of complexin-II (6 µM) (Kedar et al., 2015; Malsam et al., 2012).
316 Fusion was measured at 37°C by Atto488 fluorescence dequenching, which occurs upon lipid mixing
317 with GUVs. Calcium (100 µM free Ca^{2+} final) was added after 2 minutes to the t-SNARE GUV assay.
318 Measurements were continued for another 5 minutes. SUVs treated with botulinum toxin D, which
319 cleaves VAMP2 and abolishes membrane fusion, served as negative control and the corresponding
320 background fluorescence was subtracted. Measurements were normalized to total fluorescence
321 after detergent lysis.

322 Complexin-II clamps spontaneous Ca^{2+}-independent membrane fusion in the reconstituted assay
323 (i.e. fusion before addition of Ca^{2+}), via laterally binding the membrane-proximal C-terminal ends of
324 SNAP25 and VAMP2 (Malsam et al., 2020). Remarkably, V48F and D166Y showed impaired clamping
325 by complexin, as apparent by increased fusion before Ca^{2+} addition (Fig. 8D). The decreased
326 clamping is likely caused by the reduced interaction of V48F and D166Y with Syt1. As a note, the
327 clamping function of Syt1 becomes only obvious in the presence of complexin, whereas the
328 clamping function of complexin depends on the presence of Syt1 (Malsam et al., 2012); thus, the

329 clamping function of the two proteins cannot be separated. After Ca^{2+}-triggering, WT SNAP25
330 supported the largest amount of fusion, followed by V48F, whereas D166Y Ca^{2+}-dependent fusion
331 was clearly reduced (Fig. 8D). Notably, this is the same sequence as found for evoked release in
332 synapses, considering either the amplitude or the charge of the EPSC (Fig. 4B-C, F-G). Thus, the *in*
333 *vitro* assay reproduces both the increased spontaneous release and the reduced Ca^{2+}-dependent
334 release found in neurons, indicating that these features are present within the minimal set of fusion
335 proteins included in this assay (i.e. the SNAREs, Syt1 and complexin).

336 There is evidence that SNAP25 might enter the SNARE-complex last, after syntaxin-1 and VAMP2
337 are joined by Munc18-1 (Baker et al., 2015; Jiao et al., 2018; Sitarska et al., 2017), although another
338 view is that a syntaxin/SNAP25 dimer bound to Munc18-1 acts as an intermediary (Jakhanwal et al.,
339 2017). In the former case, mutations changing association of SNAP25 to the SNAREs might change
340 exocytosis efficiency. To test this, we used a syntaxin-1 GUV assay, where the incorporation of
341 soluble SNAP25 into the SNARE complex becomes a rate-limiting step. In this assay, fusion kinetics
342 are much slower when compared with fusion reactions containing GUVs with pre-assembled t-
343 SNAREs. Accordingly, we allowed 30 min for pre-stimulation fusion to take place, and after addition
344 of Ca^{2+} (100 µM free Ca^{2+}), fusion was followed for another 30 min (Fig. 9A). The assay was
345 performed in the presence and absence of complexin-II. D166Y and to a lesser degree V48F revealed
346 enhanced stimulation of fusion in comparison to WT before calcium was added, regardless of the
347 presence or absence of complexin (Fig. 9B). Comparing data with and without complexin established
348 that complexin barely suppressed spontaneous fusion in reactions containing the V48F mutant. The
349 presence of complexin partially reduced Ca^{2+}-independent fusion, but D166Y still stimulated pre-
350 Ca^{2+} fusion compared to wildtype. Overall, these data demonstrate that D166Y and V48F are gain-
351 of-function mutants under conditions where SNAP25 association to the other SNAREs is rate
352 limiting.

353 To test directly whether V48F and especially D166Y enhance SNARE interactions, co-flotation assays
354 were performed. SUVs containing either syntaxin-1 (Stx-1), or VAMP2, or Syt1, or the Syt1/VAMP2
355 combination were incubated with SNAP25 and re-isolated by flotation using a Nycodenz density
356 gradient. An additional reaction, reflecting the fusion assay, contained SNAP25 in combination with
357 both Syt1/VAMP2 SUVs and Syntaxin-1 SUVs (Fig. 9D). SNAP25 recruitment for each condition was
358 determined by SDS PAGE followed by Coomassie blue and silver staining. Silver stained SNAP25

359 bands were quantified, and the mutants were plotted relatively to the wildtype SNAP25 (Fig. 9D and
360 Fig. 9 – Figure supplement 1).

361 SNAP25 WT did not show any binding to Syt1 SUVs (Fig. 9 – Figure supplement 1) , although direct
362 interactions with Syt1 would be predicted based on the primary interface, indicating that such
363 interactions are not stable under the employed conditions, which is expected because SNAP25 is
364 unstructured until it binds its SNARE partners (Fasshauer et al., 1997). D166Y showed profoundly
365 increased interactions with SUVs containing either syntaxin-1, or VAMP2, or Syt1/VAMP2, and the
366 combination used in the fusion assay (Fig. 9D; Fig. 9 – Figure supplement 1). V48F displayed mildly
367 increased binding to syntaxin-1 and Syt1/VAMP1 SUVs, and a tendency to increased association to
368 VAMP2 SUVs (p=0.0629, one-sample t-test). These data show that loss of Syt1 interaction upon
369 mutation in the primary interface can be accompanied by a gain-of-function phenotype stimulating
370 interactions with the other SNARE-partners. This association of SNAP25 to the other SNAREs might
371 happen as one of the last steps towards fusion; consequently, when D166Y and V48F join the
372 complex prematurely, it will bypass layers of control and result in uncontrolled fusion.

373 *The I67N mutation supports an intact RRP, but an increased energy barrier for fusion*

374 We next addressed the phenotype of the I67N disease mutation, which was found in an 11-year-old
375 female, who suffered from myasthenia, cortical hyperexcitability, ataxia and intellectual disability,
376 but with normal brain MRI (Shen et al., 2014). The I67 is found within the interaction layer +4
377 (Fasshauer et al., 1998), which helps in assembly of the C-terminal of the SNARE-complex (Gao et
378 al., 2012), and it might therefore have a different synaptic phenotype than V48F and D166Y.

379 In *in vitro* experiments, SNARE-complexes formed with the I67N mutant displayed a lower stability,
380 with the melting temperature reduced from 71°C to approximately 56°C (Fig. 8A), as expected for a
381 mutation that destabilizes the SNARE-complex. I67N also showed a strong decrease in SUV docking
382 (Fig. 8B-C), which is likely caused by the destabilization of the t-SNARE complex, which indirectly
383 perturbs the Syt1 binding interface(s). In lipid mixing assays, I67N strongly reduced both Ca^{2+}-
384 independent and Ca^{2+}-dependent fusion, whether the t-SNAREs were preassembled (Fig. 8D-E) or
385 not (Fig. 9B-C). The co-flotation assay did not display any binding of I67N to t-SNAREs or Syt1 (Fig.
386 9D). The binding to Syt1/VAMP2 SUVs was reduced compared to SNAP25 WT, but since binding of

387 the WT protein is already very low, the biological significance of this result is unclear. Overall, these
388 data indicate that I67N is inferior in membrane fusion.

389 Lentiviruses encoding the I67N mutant N-terminally fused to EGFP expressed similar amounts as WT
390 EGFP-SNAP25 (Fig. 10A). Expression in SNAP25 KO neurons resulted in reduced rescue of survival in
391 neurons expressing I67N alone, whereas neurons co-expressing WT and I67N had intermediate
392 survival, not significantly different from WT (Fig. 10C). Staining against MAP2 (dendritic marker) and
393 VGlut1 (synapse marker) showed that the number of synapses on average was reduced in the I67N
394 (Fig. 10B,D), and the dendritic length was on average reduced, but the changes did not reach
395 statistical significance (Fig. 10E). Patch-clamp measurements demonstrated strongly reduced
396 spontaneous release frequencies (Fig. 10F-H) and evoked release amplitude (Fig 10I-L) with the I67N
397 mutation, see also (Alten et al., 2021). mEPSCs were absent in most I67N expressing neurons,
398 whereas WT and I67N co-expressing neurons had a very low mEPSC rate, much closer to the I67N
399 than the WT phenotype; similar for EPSC amplitudes (Fig. 10I-L). The I67N therefore is dominant-
400 negative for both types of release, in contrast to the incompletely dominant phenotypes of the V48F
401 and I166Y mutants (see above). The fraction of synchronous release was unchanged in WT and I67N
402 coexpressing neuron (Fig. 10L); this number could not be estimated for I67N-expressing neurons
403 due to the low amount of release.

404 Reduced spontaneous and evoked release could result from a decrease in priming, or fusion, or
405 both. To distinguish between these possibilities, we turned to sucrose applications. Application of
406 0.25M sucrose did not lead to any measurable release in I67N expressing cells, and only minimal
407 release in cells co-expressing WT and I67N (Fig. 11A-D). This indicates that the energy barrier is
408 increased in amplitude, and therefore the RRP might be underestimated when probed by 0.5M
409 sucrose (Schotten et al., 2015). Indeed, 0.5M sucrose displayed reduced release in the I67N and
410 WT+I67N condition (Fig. 11C), but this could be due to defects in priming or fusion. To investigate
411 this, we applied a stronger stimulus, 0.75M sucrose, to these cells (Schotten et al., 2015). Strikingly,
412 the RRP as assessed by 0.75M sucrose ($RRP_{0.75}$) was unchanged between WT, I67N and WT+I67N co-
413 expressed cells (Fig. 11E,G). Application of 0.375M sucrose led to small amounts of release in the
414 I67N, but more in the WT+I67N co-expressed situation (Fig. 11E,F). Forming the ratio
415 $RRP_{0.375}/RRP_{0.75}$ revealed a statistically significant reduction in I67N compared to WT (Fig. 11H).
416 Therefore, the RRP *per se* appears intact in the I67N (when probed by sufficiently high

417 concentrations of sucrose), but the vesicles face a higher apparent fusion barrier, which makes the
418 RRP appear smaller if assessed by 0.5M sucrose. The higher apparent fusion barrier explains the
419 lower frequency of mEPSC in the I67N mutation, the lower degree of spontaneous fusion in *in vitro*
420 assays, as well as the lower amount of Ca^{2+}-dependent release in vitro and in the cell.

421 The I67N mutation profoundly affected trains in 2 mM extracellular Ca^{2+} (Fig. 11I) leading to strong
422 facilitation, which is expected due to the strong phenotype of this mutation, which radically lowers
423 release probability. Even when co-expressed with WT protein, the train facilitated over the first
424 several stimulations, attesting to the strong dominant-negative feature of the I67N mutation (Fig.
425 11I-J). Consequently, the paired-pulse ratio was increased in the I67N and intermediate in the
426 WT+I67N condition (Fig. 11K). Back-extrapolation of these trains was not reliable, because the low
427 release probability in the I67N mutation made it impossible to achieve sufficient depletion of the
428 RRP.

429 The energy barrier for fusion is exquisitely sensitive to the charges on the surface of the SNARE-
430 complex, with positive charges decreasing and negative charges increasing the fusion barrier
431 amplitude (Ruiter et al., 2019). To investigate whether the same electrostatic mechanism applies to
432 the I67N, we combined the I67N mutation with a mutation of four amino acids ("4K"=SNAP25
433 E183K/S187K/T190K/E194K) in the second SNARE-domain of SNAP25, constructing the quintuple
434 mutation ("I67N/4K"=SNAP25 I67N/E183K/S187K/T190K/E194K). The 4K mutation lowers the
435 energy barrier for fusion by increasing the charge of the SNARE-complex surface by +6 via charge
436 introduction and charge reversal (Ruiter et al., 2019). The 4K-mutation increased the mEPSC release
437 rate compared to WT (Ruiter et al., 2019), whereas in the combined I67N/4K mutation the
438 spontaneous release rate was indistinguishable from WT (Fig. 12A-C), showing that increased
439 positive charges rescued the defect of spontaneous release in the I67N mutant. Evoked release was
440 also increased in the 4K mutation compared to WT (Ruiter et al., 2019), but in the I67N/4K mutation,
441 evoked release was still strongly depressed compared to WT (Fig. 12D-E). Nevertheless, evoked
442 release was noticeable in the combined mutation, whereas it was almost absent in I67N-expressing
443 cells (comp. Fig. 10I-L), indicating a positive effect of the 4K mutation, which amounted to an
444 increase by a factor ~5 (eEPSC amplitude, I67N: 0.0475 ± 0.0087; I67N/4K: 0.2668 ± 0.12 nA; Mann-
445 Whitney test, P=0.035).

446 We previously created a simple mathematical model that links the release rate to the number of
447 charges added to the SNARE-complex (Ruiter et al., 2019). This model includes both spontaneous
448 and evoked release, which are separated by the addition of 35 positive charges in the latter case
449 (Fig. 12F, black points are WT spontaneous and evoked release rates; blue line is the model fitted to
450 WT data). Placing the spontaneous release rates for I67N and I67N/4K on this curve (by dividing the
451 spontaneous release rate with RRP size and finding a corresponding charge-value using the model)
452 resulted in two points (red) separated by 5.6 charges, which is close to the nominal 6 charges added
453 by the 4K mutation (Fig. 12F). Similarly, evoked release in the I67N and the I67N/4K were separated
454 by 5.9 charges (Fig. 12F). The fact that these numbers are close to the nominal 6 charges introduced
455 shows that even for the I67N mutation, the same basal electrostatic model still applies, but the
456 deleterious effect of the I67N on evoked release rates is larger than on spontaneous rates and
457 therefore the rescue of evoked release rate by positive charges is insufficient to reach WT values.
458 Moreover, because of the saturating form of the curve (i.e. the model) adding positive charges is an
459 effective way of rescuing spontaneous, but not evoked release.

460 Overall, the I67N disease mutation increases the amplitude of the energy barrier for fusion, and it
461 does so more for evoked than for spontaneous release, but the electrostatic mechanism, which we
462 assume is part of release triggering (Ruiter et al., 2019), appears to be intact.

463 ## Discussion

464 We have shown that two SNAP25 mutations (V48F, D166Y) that compromise interaction with Syt1
465 lead to complex phenotypes characterized by a combination of loss-of-function and gain-of-function
466 features. Thereby, the mutations fall into the 'neomorph' category, where the mutated protein has
467 novel or changed interactions or functions (Verhage and Sorensen, 2020). In contrast, the I67N
468 substitution within the SNARE-bundle is a dominant-negative mutation.

469 *SNAP25 disease mutations change protein-protein interactions and the energy landscape of fusion*

470 Both the V48F and the D166Y resulted in a decrease in the amplitude of the apparent energy barrier
471 for fusion, whereas the I67N increased the amplitude of the apparent fusion barrier. A vesicle's
472 release willingness can only be assessed by fusing it; therefore, it is not possible to distinguish
473 between effects on the fusion barrier *per se*, and effects on the fusion machinery. In recognition of
474 this fact, we here refer to the "apparent energy barrier". Using Arrhenius' equation to convert
475 fusion, priming and depriming rates to their respective energy barrier heights (see Materials and
476 Methods for the assumptions behind this procedure), we can derive the energy landscape for fusion
477 of the three mutants (Fig. 13A-D). This shows the multiple changes in the V48F and D166Y, which
478 affect at least two different barriers (priming and fusion, Fig 13A-B), leading to a complex
479 phenotype, whereas for I67N the fusion barrier is primarily (or solely) affected (Fig. 13D).

480 When combining the I67N with the 4K-mutation, which introduces 6 extra positive fixed charges,
481 we could place our data within the framework of our model for electrostatic triggering (Ruiter et al.,
482 2019) and show that the effect of charge *per se* is approximately the same in the I67N mutant as in
483 the WT. Note that there are endogenous positively charged amino acids towards the C-terminal end
484 of SNAP25 that are important for release rates (Fang et al., 2015). Rescue of spontaneous release
485 was completed by adding 6 positive charges, which is consistent with the idea that the assembly of
486 the C-terminal end of the SNARE-complex, which is compromised by I67N (Rebane et al., 2018),
487 works against the electrostatic energy barrier, which is affected by the SNARE surface charge (Ruiter
488 et al., 2019). In contrast, rescue of evoked release by charges were incomplete, due to the larger
489 effect of I67N on evoked release, combined with the shallow effect of charges on evoked release
490 (Ruiter et al., 2019). The larger susceptibility of evoked release to C-terminal mutation of the

491 SNAREs might be partly due to the higher number of SNARE-complexes involved in evoked than in
492 sustained/spontaneous release (Mohrmann et al., 2010).

493 The effect of the I67N mutation in the energy domain at rest can be calculated from the
494 spontaneous release rate, which was reduced by a factor 22.4 (from 1.31 ± 0.36 to 0.0583 ± 0.0274
495 Hz). This corresponds to an effect in the energy domain of 3.1 k_BT (where k_B is Boltzmann's constant;
496 assuming unchanged RRP size, pool normalization is not required). Work with single-molecular
497 optical tweezers showed that the I67N mutation destabilizes the overall SNARE C-terminal and
498 linker domain, which are supposed to deliver the power stroke for membrane fusion, by 14 k_BT
499 (Rebane et al., 2018), which is substantially more. The reduction in spontaneous release rate is more
500 comparable to the reduction in the transition rate of folding by the C-terminal and linker domain by
501 a factor of ~10 (Rebane et al., 2018). Since at least three SNARE-complexes, possibly more,
502 contribute to vesicle fusion (Bao et al., 2018; Manca et al., 2019; Mohrmann et al., 2010; Shi et al.,
503 2012), folding kinetics correlates better to spontaneous fusion rates than overall SNARE-complex
504 stability.

505 The D166Y and V48F mutations lead to increases in spontaneous release, and more asynchronous
506 EPSCs, consistent with their localization in the primary SNARE:Syt1 interface (Schupp et al., 2016;
507 Zhou et al., 2015; Zhou et al., 2017), and the demonstrated impaired Syt1 binding (Fig. 8B-C), see
508 also (Alten et al., 2021). These phenotypes are at first glance similar to Syt1 knockout/knockdown
509 (Bouazza-Arostegui et al., 2022; Chang et al., 2018; Huson et al., 2020; Ruiter et al., 2019). However,
510 when normalized to the RRP size, mEPSC frequencies were much higher in the V48F and the D166Y
511 than in the *Syt1* KO (Fig. 6D), and dual sucrose applications indicated a decrease in the amplitude of
512 the sucrose-probed apparent energy barrier and increased release probability, features not found
513 in the *Syt1* KO (Bouazza-Arostegui et al., 2022; Huson et al., 2020). This indicates a gain-of-function
514 feature of these mutations, which fulfills D166Y>V48F; such a feature was identified as an increased
515 interaction of V48F and D166Y with VAMP2- and syntaxin-1-containing SUVs (Fig. 9D); the
516 interaction was stronger for D166Y than for V48F. AlphaFold prediction of the SNAP25 mutants did
517 not reveal major structural changes in the SNAP25 backbone. However, the replacement of D166
518 with Y shows stronger interactions with the neighboring H162 and V48F alters the interactions with
519 the neighbouring E52 (Fig. 9 - Figure supplement 2; (Jumper et al., 2021; Mirdita et al., 2022)). This
520 may result in stabilization of a structure consistent with SNARE-complex formation. However, note

521 that the AlphaFold prediction is identical to the structure of SNAP25 in the assembled SNARE-
522 complex (Zhou et al., 2015), whereas unassembled SNAP25 is likely less structured or unstructured
523 (Fasshauer et al., 1997). Overall, these disease mutants do not only fail in their interaction with Syt1,
524 they bypass fusion control, resulting in premature SNARE-complex assembly. Although the
525 increased spontaneous release rate might cause patient symptoms, Alten et al. (2021) suggested
526 that the resulting postsynaptic depolarization might compensate for the smaller EPSC amplitude to
527 normalize the overall firing rate.

528 In a SUV:GUV fusion assay, where folding of SNAP25 onto syntaxin-1/VAMP2 is rate-limiting, D166Y
529 and V48F caused an increase in pre-stimulation fusion rates. This is consistent with recent data
530 showing that folding of SNAP25 onto a template formed by VAMP2 and syntaxin-1 held in place by
531 Munc18-1 might be a late, rate-limiting, step in exocytosis (Jiao et al., 2018). This process is
532 regulated and sped up by Munc13-1 (Kalyana Sundaram et al., 2021; Shu et al., 2020; Wang et al.,
533 2019). The fact that a similar effect on spontaneous fusion was seen in the assay with preformed t-
534 SNAREs in the presence of complexin indicates that there is an assembly step, even in that assay,
535 which can be sped up by the mutations. This aligns with the demonstration by single molecule FRET
536 of a further assembled ('tighter') state of the trans-SNARE-complex induced by Ca^{2+}-unbound Syt1,
537 which becomes committed for fusion once Ca^{2+} binds (Das et al., 2020).

538 *V48F and D166Y change the size of the RRP via effects on priming, depriming and fusion*

539 We found that V48F and D166Y cause a decrease in RRP size, whether measured by sucrose
540 application or by train stimulation. The reduced RRP is at variance with the publication by Alten et
541 al., who used sucrose application to larger mixed cultures (Alten et al., 2021). There might be two
542 reasons for this discrepancy. First, Alten et al. used longer duration of sucrose application (~1 min)
543 and applied sucrose to a large mixed culture, which might result in a variable delay such that all
544 synapses are not stimulated simultaneously. This will result in temporally overlapping release of RRP
545 and upstream vesicle pools, which then cannot be distinguished from each other. Indeed, the RRP
546 size reported by Alten et al. is ~10-fold larger than RRPs measured from autaptic neurons. When
547 grown on 50-µm micro-islands, sucrose can be applied acutely (within ~0.05 s) to the entire
548 dendritic tree and all synapses using a local perfusion system, which allows distinguishing the RRP
549 from upstream pools. Second, it was recently shown that sufficient neuronal maturation is

550 necessary to detect the decrease in RRP upon Syt1 elimination (Bouazza-Arostegui et al., 2022),
551 which is likely modulated by the presence of other neurons (Chang et al., 2018; Liu et al., 2009;
552 Wierda and Sorensen, 2014). This adds an additional layer of complexity, since neuronal maturation
553 likely varies between laboratories, or even over time within the same laboratory.

554 Dissection of the three rates that determine RRP size (priming, depriming and fusion rates) showed
555 that all three are changed in the V48F and D166Y mutations. Especially for D166Y, but also for V48F,
556 spontaneous release contributed to RRP depletion by triggering premature fusion. Significant RRP
557 depletion has not been expected for moderate increases in mEPSC frequency (Rhee et al., 2005;
558 Ruiter et al., 2019), based on the argument that RRP refilling should be fast enough to counteract
559 depletion. However, to properly make this argument, priming, depriming and spontaneous release
560 rates must be compared in the steady-state situation. Similarly, we recently showed by cryo-
561 electron tomography that the 4K-mutation, which increased the mEPSC frequency to ~30 Hz and
562 had a reduced RRP (Ruiter et al., 2019) caused a loss of synaptic vesicles tethered to the membrane
563 with three tethers (Radecke et al., 2023), which is the structural correlate of the RRP (Fernandez-
564 Busnadiego et al., 2010).

565 The major effect on RRP size is caused by a reduction in forward priming rate by D166Y and V48F.
566 Comparison to the Syt1 KO showed qualitatively similar changes, but of a smaller magnitude, with
567 spontaneous release playing a negligible role for RRP size. Notably, in all three cases a reduction in
568 depriming rate partly counteracted the lowered priming rate (Table 1) – this was only significant for
569 D166Y. Indeed, part of the role of Syt1:SNARE interaction might be catalytic, lowering the energy
570 level of a transition state along the path to priming, which will affect both rates (Walter et al., 2013).
571 This might happen because transient binding to Syt1 might structure SNAP25 and assist in formation
572 of the SNARE-complex, whereas SNAP25 mutants might prestructure the protein, bypassing the
573 need for Syt1. In an energy diagram (Fig. 13) it becomes clear that vesicle priming and regulation of
574 spontaneous release are interdependent. Stabilization of the RRP state will both increase RRP size
575 at rest and reduce spontaneous release, since lowering the energy level of (i.e. stabilizing) RRP
576 vesicles will increase the size of the energy barrier that the RRP vesicles face (Fig. 13). Consistently,
577 downregulation (clamping) of spontaneous release and upregulation of evoked release are often
578 interdependent under conditions where Syt1 expression level, or Syt1 interaction with the SNAREs,
579 are up or down regulated (Courtney et al., 2021; Courtney et al., 2019; Vevea and Chapman, 2020;

580 Zhou et al., 2015; Zhou et al., 2017). This does not rule out the existence of mutations that can affect
581 one mode of release more than the other (e.g. the I67N/4K mutation). By inference, assembly of
582 the primary Syt1:SNARE interface (Zhou et al., 2017) is most likely involved in both clamping release
583 and setting up a RRP. In further support of this, the minimal *in vitro* assay with preassembled t-
584 SNARE dimers displayed a qualitatively similar reduction in calcium-dependent release, with D166Y
585 being more impaired than V48F (Fig. 8D). Overall, the energetic contribution of Syt1:SNARE
586 interaction to Ca^{2+}-triggered release is a stabilization of upstream steps, and the increase of the
587 fusion barrier downstream of the RRP (Fig. 13). The electrostatic nature of the fusion barrier (Ruiter
588 et al., 2019) ensures its rapid dissolution by Ca^{2+}, possibly by unbinding of Syt1 from the SNARE
589 complex (Voleti et al., 2020).

590 For the I67N-mutation, the sucrose-RRP was also reduced in size when using 0.5 M sucrose, which
591 is consistent with previous observations (Alten et al., 2021). However, when the energy barrier for
592 release is increased, 0.5 M sucrose is insufficient to deplete the RRP (Schotten et al., 2015).
593 Accordingly, 0.75 M sucrose released an RRP of similar size in WT, I67N and I67N+WT co-expressing
594 cells, showing that the vesicle priming reaction is intact, but the vesicles face a larger fusion barrier
595 (Fig. 11). In this mutant, train stimulations in the I67N or co-expressed WT + I67N case resulted in a
596 phenotype quite distinct from the WT, with strong facilitation throughout the train. Thus, the I67N
597 is a strongly dominant-negative mutant, whether considering mEPSC frequency, eEPSC amplitude
598 or train stimulations, whereas V48F and D166Y are incompletely dominant. This can be explained
599 by the different function of SNAP25 domains during fusion, where V48 and D166 help set up an
600 arrested primed vesicle state by interacting with Syt1 (Schupp et al., 2016; Zhou et al., 2015; Zhou
601 et al., 2017), whereas I67N participates in the final conformational change, the 'stroke' that leads
602 to assembly of the C-terminal end of the complex and the linker domain. Due to their defect in
603 priming, V48F and D166Y might not enter the super-complex (the complex of SNARE-complexes
604 driving fusion) as often as WT protein. In contrast, I67N will readily enter the super-complex and
605 compromise its function, which will lead to a dominant-negative phenotype due to the multiple
606 SNARE-complexes involved in fusion (Bao et al., 2018; Mohrmann et al., 2010; Shi et al., 2012).

607 Back-extrapolation of 40 Hz trains (@4 mM Ca^{2+}) also led to the conclusion that V48F and D166Y
608 have a reduced RRP_{ev}, the RRP-subpool that action potentials draw on, and a reduced forward
609 priming rate. Interestingly, the release probability when normalized to the sucrose pool ($RRP_{0.5}$) was

610 increased non-significantly for the V48F and significantly for the D166Y mutation, but when
611 considering 40Hz trains, the release probabilities of both mutations were decreased, consistent with
612 a shift towards facilitation. The latter finding is likely caused by the defective interaction with Syt1,
613 which leads to suboptimal priming and/or defective super-priming, which is an additional priming
614 step after entry of the vesicle into the RRP (Lee et al., 2013; Taschenberger et al., 2016). This will
615 lead to reduction of the first EPSC of a train and thereby a lowered nominal release probability.
616 However, when comparing the EPSC charge to the $RRP_{0.5}$, the strong reduction in the $RRP_{0.5}$ pool
617 (especially in the D166Y mutation) accounts for the increase in the overall release probability. This
618 can be explained if spontaneous release causes a disproportional depletion of vesicles, which are in
619 the $RRP_{0.5}$, but not in the RRP_{ev}.

620 *Conclusion*

621 SNAP25 disease missense mutations change the function of the protein without compromising its
622 expression, leading to dominant negative or neomorphic mutations. Missense mutations in the
623 primary SNARE:Syt1 interface (V48F, D166Y) result in a complex phenotype characterized by loss-
624 of-function in the priming step and gain-of-function in the fusion step. Missense mutation in the
625 SNARE-bundle (I67N) leads to an increased amplitude of the energy barrier for fusion. In addition,
626 disease mutations display inefficient rescue of neuronal survival. Overall, SNAP25 encephalopathy
627 caused by single missense point mutations presents with interdependent functional deficits, which
628 must be overcome for successful treatment.

629

630 ## Materials and Methods

631 *Animals*

632 SNAP25 KO C57/Bl6-mice: Heterozygous animals were routinely backcrossed to Bl6 to generate new
633 heterozygotes. The strain was kept in the heterozygous condition and timed pregnancies were used
634 to recover knockout embryos by caesarean section at embryonic day 18 (E18). Pregnant females
635 were killed by cervical dislocation; E18 embryos of either sex were collected and killed by
636 decapitation. Permission to keep and breed *Snap25* and *Syt1* mice was obtained from the Danish
637 Animal Experiments Inspectorate (2018-15-0202-00157) and followed institutional guidelines as
638 overseen by the Institutional Animal Care and Use Committee (IACUC). CD1 outbred mice were used
639 to create astrocytic cultures and mass cultures for Western blotting. Newborns (P0-P2) of either sex
640 were used. Pups were killed by decapitation.

641 *Cell lines*

642 HEK293-FT cells for production of lentiviruses were obtained from the Max-Planck-Institute for
643 biophysical chemistry. The cells were passaged once a week, and they were used between passage
644 11 and 25 for generation of lentiviral particles. The cells were kept in DMEM + Glutamax (Gibco, cat.
645 31966047) supplemented with Fetal Bovine Serum (Gibco, cat. 10500064), Pen/Strep (Gibco, cat.
646 15140122) and Geneticin G418 (Gibco, cat. 11811064) at 37°C in 5% CO_2.

647 *Preparation of neuronal culture*

648 Self-innervating ("autaptic") hippocampal cultures were used (Bekkers and Stevens, 1991).
649 Astrocytes were isolated from CD1 outbred mice (P0-P2). The cortices were isolated from the brains
650 in HBSS-HEPES medium (HBSS supplemented with 1 M HEPES) and the meninges were removed.
651 The cortical tissue was chopped into smaller fragments, transferred to 0.25% trypsin dissolved in
652 DMEM solution (450 ml Dulbecco's MEM with 10% Foetal calf serum, 20000 IU Penicillin, 20 mg
653 Streptomycin, 1% MEM non-essential Amino Acids) and incubated for 15 min at 37 °C. Subsequently,
654 inactivation medium (12,5 mg Albumin + 12,5 mg Trypsin-Inhibitor in 5 ml 10% DMEM) was added,
655 the tissue was washed with HBSS-HEPES, triturated and the cells were plated in 75 cm^2 flasks with
656 pre-warmed DMEM solution (one hemisphere per flask) and stored at 37 °C with 5% CO_2. Glial cells
657 were used after 10 days.

658 Glass coverslips were washed overnight in 1 M HCl; for an hour in 1 M NaOH and washed with water
659 before storage in 96% ethanol. Coverslips were first coated by 0.15 % agarose and islands were
660 made by stamping the coating mixture (3 parts acetic acid (17 mM), 1 part collagen (4 mg/ml) and
661 1 part poly-D-lysine (0.5 mg/ml)) onto the glass coverslips using a custom rubber stamp. Glial cells
662 were washed with pre-warmed HBSS-HEPES. Trypsin was added and the flasks were incubated at
663 37 °C for 10 min. Cells were triturated and counted in a Bürker chamber before plating onto the
664 glass coverslip with DMEM solution. After 2-5 days, neurons were plated on the islands.

665 Neurons for autaptic culture were isolated from E18 *Snap25* KO mice. Pups were selected based on
666 the absence of motion after tactile stimulation and bloated neck (Washbourne et al., 2002); the
667 genotype was confirmed by PCR in all cases. The cortices were isolated from the brains in the HBSS-
668 HEPES medium. The meninges were removed and the hippocampi were cut from the cortices before
669 being transferred to 0.25% trypsin dissolved in HBSS-HEPES solution. The hippocampi were
670 incubated for 20 min at 37 °C, subsequently washed with HBSS-HEPES, triturated and the cell count
671 was determined with a Bürker chamber before plating on the islands (7000-8000 neurons per well).
672 Cells were incubated in the NB medium (Neurobasal with 2% B-27, 1 M HEPES, 0,26% Glutamax,
673 14,3 mM β-mercaptoethanol, 20000 IU Penicillin, 20 mg Streptomycin) and used for measurements
674 between DIV10-14.

675 Hippocampal neurons for high-density cell culture for Western blotting were obtained from P0-P1
676 CD1 outbred mice. The dissection, tissue digestion and cell counting were performed the same way
677 as the neurons for the autaptic culture, the high-density culture (600,000 neurons per well) was
678 then kept in NB-A medium (Neurobasal-A with 2% B-27, 1 M HEPES, 0,26% Glutamax, 20000 IU
679 Penicillin, 20 mg Streptomycin) and half the volume of the media was replaced every 2-3 days before
680 harvesting the cells at DIV14.

681 *Constructs for rescue experiments*

682 SNAP25B was N-terminally fused to GFP and cloned into a pLenti construct with a CMV promoter
683 (Delgado-Martinez et al., 2007). Mutations were made using the QuikChange II XL kit (Agilent).
684 Primers were ordered from TAGC Copenhagen. All mutations were verified by sequencing before
685 virus production. Viruses were prepared as previously described using transfection of HEK293FT-

686 cells (Naldini et al., 1996). Neurons were infected with lentiviruses on DIV 0-1. 30 µl total virus per
687 well (WT or mutant; 15 µl + 15 µl WT + mutant virus for co-expressed condition).

688 *Immunostaining and confocal microscopy*

689 Autaptic hippocampal neurons were fixed at DIV14 in 2% PFA in culture medium for 10 min and
690 subsequently in 4% PFA for 10 min. Cells were then washed with PBS, permeabilized by 0.5% Triton
691 X-100 for 5 min and blocked with 4% normal goat serum in 0.1% Triton X-100 (blocking solution) for
692 30 min. Cells were incubated with primary antibodies diluted in blocking solution (anti-MAP2, 1:500,
693 chicken, ab5392, Abcam; and anti-vGlut1 1:1000, guinea pig, AB5905, Merck Millipore) for 2 h at RT.
694 After washing with PBS, the cells incubated with secondary antibodies in blocking solution for 1h at
695 RT in the dark (anti-chicken Alexa 568, 1:1000, A11041, Thermo Fisher Scientific; and anti-guinea
696 pig Alexa 647, 1:1000, A-21450, Thermo Fisher Scientific) and washed again. Coverslips were
697 mounted with FluorSave and imaged on Zeiss CellObserver spinning disc confocal microscope (40x
698 water immersion objective; NA 1.2) with Zeiss Zen Blue 2012 software. Images were acquired as Z-
699 stack and 9 images per plane to capture the whole island in the field of view. The images were post-
700 processed with Zeiss Zen Black software and neuronal morphology was analyzed using SynD
701 automated image analysis (Schmitz et al., 2011).

702 *Western Blotting*

703 Harvesting the high-density hippocampal culture, BCA assay and transferring the protein samples
704 on a PVDF membrane were performed as described before (Ruiter et al., 2019). Incubation in
705 primary antibodies (a-SNAP25: mouse, 1:10000, SYSY 111011, Synaptic Systems; a-VCP: mouse,
706 1:2000, ab11433, Abcam) was performed overnight with 70 rpm shaking at 4 °C, followed by
707 washing in TBST (0.1%) and a 1 h incubation in secondary antibody (goat a-mouse-HRP: 1:10000,
708 P0447, Dako). After washing, Pierce ECL Western blotting substrate was added and
709 chemiluminescence was visualized with FluorChem E (Proteinsimple).

710 *Electrophysiology*

711 Autaptic cultures were used from DIV10 until DIV14. The intracellular pipette medium contained:
712 KCl 136 mM, HEPES 17.8 mM, Creatine Phosphate 15 mM, Na-ATP 4 mM, Creatine Phosphokinase
713 50 U, $MgCl_2$ 4.6 mM, EGTA 1 mM (pH 7.4, osmolarity ~300 mOsm). The standard extracellular

714 recording medium contained: NaCl 140 mM, KCl 2.4 mM, HEPES 10 mM, Glucose 14 mM, $CaCl_2$ 2
715 mM, $MgCl_2$ 2 mM. The extracellular recording medium for de-priming experiments contained: NaCl
716 140 mM, KCl 2.4 mM, HEPES 10 mM, Glucose 14 mM, $CaCl_2$ 4 mM, $MgCl_2$ 4 mM (pH 7.4, osmolarity
717 ~300 mOsm). An Axio Observer A1 inverted microscope (Zeiss) was used to visualize the cells. The
718 recordings were performed at room temperature. An EPC10 amplifier (HEKA) was used with the
719 program Patchmaster v2.73 (HEKA). Traces were filtered with a 3kHz Bessel low-pass filter and data
720 were acquired at 20 kHz. The series resistance was compensated to 70%. Glass pipettes were freshly
721 pulled on a P1000 pipette puller (Sutter Instruments) from borosilicate glass capillaries. Pipets
722 ranging from 2.5 to 5 MΩ were selected for recordings. Cells with starting access resistance above
723 10 MΩ were rejected. Recordings were performed in voltage clamp, with the holding potential kept
724 at -70 mV. Evoked excitatory postsynaptic currents (EPSC) were induced by raising the holding
725 voltage to 0 mV for 2 ms. Sucrose was dissolved into the standard extracellular recording medium.
726 Application of the extracellular media was done using a custom-made barrel system, controlled by
727 SF-77B perfusion fast step (Warner Instruments) controlled via digital output switches from the
728 EPC10. Electrophysiological data was analyzed in IGOR Pro (v6.21 and v6.37, WaveMetrics) using a
729 custom-written script. mEPSCs were analyzed with MiniAnalysis (v6.0.7, Synaptosoft).

730 *Electrophysiological data: Calculations*

731 Deconvolution was calculated and the electrostatic model for triggering was fitted to 4K and
732 I67N/4K data as described before (Ruiter et al., 2019). Since the evoked release for I67N was so
733 small that deconvolution became unreliable, we downscaled the peak release rate of the I67N/4K
734 mutation with a factor of 5.616, corresponding to the reduction in eEPSC amplitude in the I67N
735 compared to I67N/4K.

736 In order to determine the reasons for the reduced RRP size for V48F and D166Y, we considered a
737 single pool model for the RRP, with priming rate k_1, depriming rate k_{-1}, and fusion rate k_f (Fig. 6A).
738 The equation describing the evolution in RRP size is:

739 (Eq. 1) $$\frac{d\mathrm{RPP}(t)}{dt} = k_1 - \left(k_{-1} + k_f\right) \cdot \mathrm{RRP}(t)$$

740 where k_1 has the unit vesicles/s, whereas k_{-1}, and k_f have the unit 1/s. The solution of this differential
741 equation is

742 (Eq. 2) $$\mathrm{RPP}(t) = \frac{k_1}{(k_{-1}+k_f)}\left(1 - e^{-(k_{-1}+k_f)t}\right)$$

743 The steady-state RPP size is

744 (Eq. 3) $$RRP = \frac{k_1}{(k_{-1}+k_f)}$$

745 The miniature release rate at steady state is

746 (Eq. 4) $$r_{mini} = \frac{k_f k_1}{(k_{-1}+k_f)}$$

747 When stimulated by sucrose, k_f increases, and if $k_f >> k_{-1}$ (for justification, see below) the current
748 plateau will report on the forward priming rate alone:

749 (Eq. 5a) $$r_{prime} \approx k_1$$

750 Thus, the current plateau during sucrose application can be used for estimating the forward priming
751 rate. However, application of 0.5 M sucrose causes cell shrinkage and changes in solution viscosity,
752 which in turn can change the leak current. This might cause the plateau current to change, which
753 might be invisible during the experiment due to the synaptic events. To correct for this, we
754 implemented variance-mean analysis to identify the true baseline current (the current
755 corresponding to the lack of synaptic release). Synaptic release is essentially a source of shot noise,
756 for which the variance is proportional to the mean. We therefore calculated the variance (after
757 subtraction of a running average) and mean of the current in 50 ms intervals during the sucrose
758 application, and performed linear regression in a variance-mean plot. The corrected baseline was
759 identified by backextrapolation to the variance level found in the absence of synaptic activity (using
760 a stretch of current before sucrose application), as illustrated in Fig. 6C.

761 If sucrose does not sufficiently increase k_f, the equation 5a above would be replaced by

762 (Eq. 5b) $$r_{mini} = \frac{k_f k_1 N_{suc}}{\left(k_{-1} + k_f N_{suc}\right)}$$

763 where N_{suc} is the fold-increase in k_f induced by sucrose application. Plotting the solutions to Eqs 3,
764 4, and 5b at different values of N_{suc}, the dependency of the estimated k_{-1} and k_1 upon N_{suc} can be
765 investigated (Figure 6 – Figure supplement 1). Notably, in wildtype cells N_{suc} >5,000 (Schotten et al.,
766 2015), indicating that the estimated values of k_{-1} and k_1 using Eq. 5a (Table 1) is quite accurate for

767 the WT case, and the estimation in the case of the D166Y and V48F is even less dependent on N_{suc},
768 because the value of k_f is higher at rest (Figure 6 – Figure supplement 1). Importantly, for no realistic
769 value of N_{suc} would the conclusion of decreased k_1 and k_{-1} in the two mutants be in jeopardy.

770 For calculating the energy profiles of WT and mutants, we used Arrhenius' Equation:

771 (Eq. 6) $$k = Ae^{(\frac{-E_A}{RT})}$$

772 where E_A is the activation energy, R and T are the gas constants and the absolute temperature,
773 respectively, and A is an empirical constant that depends on collision rates (Schotten et al., 2015).
774 Solving for the activation energy, we get:

775 (Eq. 7) $$E_a = RT(\ln(A) - \ln(k))$$

776 Since A is unknown, we cannot use this equation to calculate the absolute values of the transition
777 energies; however, when we compare a mutation to the WT condition, and under the assumption
778 that A is unchanged by mutation, we can calculate the difference in energy level of the transition
779 states:

780 (Eq. 8) $$\Delta E_a^{Mut-WT} = RT(\ln(k^{WT}) - \ln(k^{Mut}))$$

781 Using this equation sequentially, for the priming rate, the depriming rate and the fusion rate, we
782 can derive the entire energy diagram, under the additional assumption that the energy in the pre-
783 primed state is identical between WT and mutation, and using that at room temperature, RT=2.479
784 kJ/mol.

785 The assumption that the empiric factor, *A*, is unchanged by mutation is likely to hold for the fusion
786 reaction, which depends on conformational changes in a preformed complex. In contrast, collision
787 rates might be involved in priming; in that case, the effect of the V48F and D166Y mutations on
788 priming, which we here attribute to an increase in the energy level of the priming transition state
789 might reflect a lower collision rate between vesicles and plasma membrane fusion machinery,
790 and/or a lower energy level of the pre-primed state.

791 *Constructs for in vitro protein expression*

792 The following constructs were used: Glutathione S-Transferase (GST) - full length VAMP2 is encoded
793 by plasmid pSK28 (Kedar et al., 2015), GST-cytosolic domain VAMP2 (amino acids 1-94) (pSK74,

794 (Ruiter et al., 2019)), synaptotagmin 1-His6 lacking the luminal domain (amino acids 57-421) (pLM6,
795 (Mahal et al., 2002), His6-complexin II (CpxII) (pMDL80, (Malsam et al., 2012)), His6-syntaxin-1A
796 (pSK270, (Schollmeier et al., 2011)), His6-SNAP25B (pFP247, (Parlati et al., 1999)), t-SNARE
797 consisting of syntaxin-1A and His6-SNAP25B (pTW34, (Parlati et al., 1999)). Point mutants in soluble
798 His6-SNAP25B and in the t-SNARE complex were generated by using the DNA templates pFP247 and
799 pTW34, respectively, and the Quikchange DNA mutagenesis kit (Qiagen) (Ruiter et al., 2019).
800 Thereby, the following SNAP25 constructs were established: His6-SNAP25B mutant I67N (pUG1),
801 V48F (pUG2), D166Y (pUG3), and t-SNAREs containing the corresponding SNAP25B mutants I67N
802 (pUG7), V48F (pUG8), and D166Y (pUG9). The identity of all constructs was validated by DNA
803 sequencing.

804 *Protein expression and purification*

805 In general, the expression vectors, encoding the desired protein constructs were transfected into
806 *Escheria coli* BL21 (DE3) (Stratagene). At an OD_{660} of 0.8, protein expression was induced by the
807 addition of 0.3 mM IPTG. Alternatively, proteins were expressed by autoinduction using buffered
808 media containing lactose (Studier, 2005). Cells were harvested by centrifugation (3500 rpm, 15
809 minutes, H-12000 rotor, Sorvall) and lysed using the high-pressure pneumatic processor 110L
810 (Microfluidics). Cell fragments were removed by centrifugation at 60.000 rpm (70Ti rotor, Beckman)
811 for 1 hour and the clarified supernatant was snap-frozen in liquid nitrogen.

812 The purification of full length VAMP2 was performed as described previously (Kedar et al., 2015)
813 with the following modifications. Cells were grown in ZYM media (Studier, 2005) and protein
814 expression was induced with IPTG for 3 hours at 25°C. The purification and expression of the GST-
815 tagged cytosolic domain of VAMP2 was described previously (Ruiter et al., 2019). Synaptotagmin 1-
816 His6 lacking the luminal domain was purified as described previously (Malsam et al., 2012) with the
817 following modification. After dilution to 50 mM salt, the protein was further purified on a MonoS
818 Sepharose column (GE healthcare) applying a gradient of 50 to 500 mM KCl in 25 mM Hepes-KOH
819 (pH 7.4).

820 His6-syntaxin-1A purification was performed as outlined by (Schollmeier et al., 2011) with the
821 following modifications. Briefly, cells were grown in ZYM media (Studier, 2005) and autoinduction
822 was used for the protein expression at 22°C overnight. Syntaxin-1A was eluted from Ni-NTA-beads

823 (Qiagen) by over-night cleavage with Prescission protease (GE healthcare) at 4°C, removing the His_6
824 tag. After dilution to 80 mM salt, the protein was further purified on a MonoQ Sepharose column
825 (GE healthcare) applying a gradient of 50 to 500 mM KCl in 25 mM HEPES-KOH (pH 7.4).

826 His6-SNAP25 was expressed as depicted for syntaxin-1A and purified via Ni-NTA beads, followed by
827 MonoQ Sepharose column chromatography (Ruiter et al., 2019). Preassembled full-length t-SNARE
828 complexes were expressed and purified as described previously (Weber et al., 1998). His_6-Complexin
829 II expression and purification was performed according to (Malsam et al., 2012) with the following
830 modifications. His6-CpxII was expressed in BL21-DE3 codon+ bacteria for 2 hours at 27°C.

831 The concentrations of purified proteins were determined by SDS-PAGE and Coomassie Blue staining
832 using BSA as a standard and the Fiji software for quantification. Furthermore, mutant and wildtype
833 protein concentrations were directly compared on a single gel.

834 *Protein reconstitution into liposomes*

835 All lipids were from Avanti Polar Lipids, except of Atto488-DPPE and Atto550-DPPE, which were
836 purchased from ATTO-TEC. For VAMP2 and Syt1 reconstitution into small unilamellar vesicles
837 (SUVs), lipid mixes (3 µmol total lipid) with the following composition were prepared: 25 mol% POPE
838 (1-hexadecanoyl-2-octadecenoyl-SN-glycero-3-phosphoethanolamine), 15 mol% DOPS (1,2-
839 dioleoyl-SN-glycero-3-phosphoserine), 29 mol% POPC (1-palmitoyl-2-oleoyl-SN-glycero-3-
840 phosphocholine), 25 mol% cholesterol (from ovine wool), 5 mol% PI (L-α-phosphatidylinositol), 0.5
841 mol% Atto488-DPPE (1,2-dipalmitoyl-SN-glycero-3-phosphoethanolamine) and 0.5 mol% Atto550-
842 DPPE. For docking assays, the t-SNARE liposome lipid mix (5 µmol total lipid) had the following
843 composition: 35 mol% POPC, 15 mol% DOPS, 20 mol% POPE, 25 mol% cholesterol, 4 mol% PI, 0,05
844 mol% Atto647-DPPE and 0,5 mol% tocopherol. For the preparation of PI(4,5)P2-containing t-SNARE
845 and syntaxin-1A liposomes, the t-SNARE liposome lipid mix was used, but 1 mol% PI(4,5)P2 (L-α-
846 phosphatidylinositol-4,5-bisphosphate) was added and the POPC concentration lowered by 1%
847 accordingly.

848 Proteins were reconstituted as described previously (Malsam et al., 2012). For the docking and
849 fusion assays, t-SNARE wildtype and mutants were reconstituted at a protein to lipid ratio of 1:900.
850 For the syntaxin-1A membrane fusion assay, syntaxin-1A was reconstituted at a protein to lipid ratio
851 of 1:1000. Briefly, 5 µmol dried lipids were dissolved in 0.7 ml reconstitution buffer (25 mM HEPES-

852 KOH, pH 7.4, 550 mM KCl, 1 mM EDTA-NaOH, 1 mM DTT) containing final 1.4 weight% octyl-ß-D-
853 glucopyranoside (ß-OG) and either 6.5 nmol (390 µg) t-SNARE complex or 5 nmol (165 µg) syntaxin-
854 1A. SUVs containing either t-SNARE or syntaxin-1A were formed by rapid ß-OG dilution below the
855 critical micelle concentration by adding 1.4 ml reconstitution buffer. For the quantification of lipid
856 recovery, a 20 µl aliquot (GUV input) was removed and stored at -20°C. The liposome suspension
857 was desalted using a PD10 column (GE Healthcare) equilibrated with desalting buffer 1 (1 mM
858 HEPES-KOH, pH 7.5, 1 w/v% glycerol, 10 µM EGTA-KOH, 1 mM DTT) and snap frozen in four aliquots
859 in liquid nitrogen and stored in -80°C. These syntaxin-1A and t-SNARE SUVs were later used to
860 prepare giant unilamellar vesicles (GUVs). The final protein to lipid ratios were determined by SDS-
861 PAGE and Coomassie Blue staining of the proteins and Atto647 fluorescence intensity
862 measurements of the lipids.

863 VAMP2/Synaptotagmin 1-SUVs were prepared as described previously (Malsam et al., 2012; Weber
864 et al., 1998) with the following modification: VAMP2 and Synaptotagmin 1 were reconstituted at a
865 protein to lipid ratio of 1:350 and 1:800, respectively. SUVs, which were used for the SNAP25
866 recruitment assay, were not dialyzed twice, but directly harvested after the density gradient
867 flotation and lipid recovery and protein-to-lipid-ratio were determined (Stx1-SUVs: 1:1900; Syt1/V2-
868 SUVs: Syt1 1:700, VAMP2 1:300; V2-SUVs: VAMP2 1:200; Syt1-SUVs: Syt1 1:700).

869 *GUV preparation*

870 GUVs were prepared as described previously (Kedar et al., 2015). Briefly, t-SNARE or syntaxin-1A
871 liposomes (1.25 µmol lipid) were loaded onto a midi column (GE Healthcare) equilibrated with
872 desalting buffer 2 containing trehalose (1 mM HEPES-KOH, pH 7.5, 0.5 w/v% glycerol, 10 µM EGTA-
873 KOH, pH 7.4, 50 µM MgCl2, 1 mM DTT, 10 mM trehalose). 1.4 ml eluate were collected and
874 liposomes sedimented in a TLA-55 rotor (Beckman) at 35.000 rpm for 2 h at 4°C. The pellet was
875 resuspended by rigorous vortexing and, while vortexing, was diluted with 10 µl of pellet
876 resuspension buffer (1 mM HEPES-KOH, pH 7.4, 10 µM EGTA-KOH, 50 µM $MgCl_2$) to lower the
877 osmotic strength. The total volume (20-25 µl) was spread as a uniform layer (14 mm diameter) on
878 the surface of a platinum foil (Alfa Aesar; 25 x 25 mm, 0.025 mm thick) attached to a glass slide as
879 support. After drying the liposome suspension for 50 min at 50 mbar, the incubation chamber was
880 assembled using an O-ring (2 mm x 18 mm), filled with 620 µl of swelling buffer (1mM EPPS-KOH,

881 pH 8.0, 240 mM sucrose (Ca^{2+} free), 1 mM DTT) and closed using a second platinum plate.
882 Conductive copper tape (3M) was attached to the platinum foil to connect the assembly with a
883 function generator (Voltcraft 8202). GUVs were generated by electro-formation at 10 Hz and 1 V at
884 0°C overnight.

885 *Lipid mixing assay*

886 The membrane fusion assay was performed as described previously (Malsam et al., 2012), except
887 that in the fusion buffer HEPES was replaced with 20 mM MOPS pH 7.4. Briefly, t-SNARE-GUVs (14
888 nmol lipid, 15 $\pm$ 0,7 pmol t-SNARE) were preincubated with or without 6 µM (0,6 nmol) CpxII for 5
889 min on ice in fusion buffer containing 0,1 mM EGTA-KOH and 0.5 mM $MgCl_2$. When using syntaxin-
890 1A-GUVs (14 nmol lipid, 14 pmol syntaxin-1A), these preincubations contained 2 µM (0.2 nmol) of
891 soluble SNAP25 in addition. Subsequently, VAMP2/Syt1-SUVs (2.5 nmol lipid, 4.5 pmol VAMP2, 2
892 pmol Syt1) were added to the GUV reaction mix resulting in 104 µl sample volume. After 10 minutes
893 on ice, 100 µl of the GUV-SUV mixes were transferred into a prewarmed 96-well plate (37°C) and
894 fluorescence emitted by Atto488 (λ_{ex} = 485 nm, λ_{em} = 538 nm) was measured in a Synergy 4 plate
895 reader (BioTek Instruments GmbH) at intervals of 10 seconds. Ca^{2+} was added to a final free
896 concentration of 100 µM
897 (https://somapp.ucdmc.ucdavis.edu/pharmacology/bers/maxchelator/CaEGTA-TS.htm) after 2
898 minutes or 30 minutes for t-SNARE-GUVs or syntaxin-1A-GUVs, respectively. The fusion reactions
899 were stopped after 4 minutes for t-SNARE-GUVs or after 1 h for syntaxin-1A-GUVs by the addition
900 of 0.7% SDS and 0.7% n-Dodecyl-ß-D-Maltosid (DDM). The resulting "maximum" fluorescent signal
901 was used to normalize the fusion-dependent fluorescence. As a negative control, SUVs were treated
902 with Botulinum NeuroToxin type D (BoNT-D) and their fluorescence signals were subtracted from
903 individual measurement sets. Three independent fusion experiments were performed for each
904 mutant.

905 *SUV-GUV binding assay*

906 All SUV-GUV binding studies were performed in an ice bath and all pipetting steps were carried out
907 in the cold room to avoid membrane fusion (Parisotto et al, 2012; Malsam et al, 2012; Weber et al,
908 1998). Before starting the incubation, potential SUV aggregates were removed by centrifugation. T-
909 SNARE-GUVs (28 nmol lipid, 30 $\pm$ 1,4 pmol t-SNARE) were preincubated with VAMP2/Syt1-SUVs (5

910 nmol lipid, 9 pmol VAMP2, 4 pmol Syt1) on ice in 100 µL fusion buffer (20 mM MOPS-KOH, pH 7.4,
911 135 mM KCl, 1mM DTT) with 0.1 mM EGTA and 1 mM $MgCl_2$. After 10 min incubation, the reactions
912 were underlaid with 20 µL of a sucrose cushion (1 mM MOPS-KOH, pH 7.4, 60 mM sucrose, 1 mM
913 DTT) and the GUVs with attached SUVs were re-isolated by centrifugation for 10 min. After removing
914 the supernatant, the pellets (in 10 µL remaining volume) were resuspended, transferred into new
915 tubes, treated with 100 µL of 1% SDS/1% DDM and the SUV recovery was determined by measuring
916 the Atto488 fluorescence.

917 To determine the respective inputs, 28 nmol GUV lipids or 5 nmol SUV lipids were treated with 1%
918 SDS/1% DDM (final) and the corresponding Atto647 and Atto488 fluorescence was measured at λ_{ex}
919 = 620/40 nm, λ_{em} = 680/30 nm and λ_{ex} = 485/20 nm, λ_{em} = 528/20 nm, respectively. A sample lacking
920 SUVs was used to determine the GUV recovery (usually 80-95%). GUV recovery of each sample was
921 used to normalize the respective SUV docking. A sample without GUVs was used to determine the
922 absolute background (usually <15%), which was subtracted from all samples.

923 *SNAP25 recruitment assay / SUV flotation assay*

924 Small unilamellar liposomes (SUVs) containing 35 pmol syntaxin-1A or 210 pmol VAMP2 and/or 100
925 pmol Synaptotagmin-1 (66 nmol lipid for Stx1-, V2/Syt1- or Syt1-SUVs, 40 nmol lipid for V2-SUVs)
926 were mixed with 180 pmol SNAP25 in a final assay volume of 50 µl in fusion buffer (20 mM MOPS-
927 KOH, pH 7.4, 135 mM KCl, 1 mM DTT). After two hours on ice, allowing the SNARE complex
928 formation, the samples were diluted five times with fusion buffer and mixed with the equivalent
929 volume of 80% nycodenz solution. After overlaying the sample with 100 µl 35% nycodenz, 25 µl 20%
930 nycodenz solution and finally with 5 µl fusion buffer in an ultra-clear tube (5 x 41 mm), the liposomes
931 were isolated by centrifugation for 3 h 40 mins at 55,000 rpm at 4°C in a SW 60 rotor (SW 60 Ti,
932 Beckman). 20 µl were harvested from the top of the gradient and mixed with 8 µl of 4x Laemmli
933 buffer (final 62.5 mM Tris-HCl, pH 6.8, 10% glycerol, 2% SDS, 50 mM ß-mercaptoethanol, 0.1%
934 bromphenol blue). 18 µl of this mixture were used to quantify the amount of recruited SNAP25 by
935 SDS PAGE followed by Coomassie Staining and Silver Staining. Using the Fiji software (Image J based)
936 the Coomassie stained band intensity of syntaxin-1A or VAMP2 or Syt1, respectively, were
937 determined and normalized to the respective mean. Subsequently, Silver Staining was used to
938 quantify the band intensities of SNAP25, and these values were normalized to the intensities of the

939 relative protein (e.g. Syntaxin-1A) based on the Coomassie Staining. From this, the ratios between
940 the SNAP25 mutants and wild type were determined.

941 *Temperature-dependent dissociation of v-/t-SNARE complexes in SDS*

942 SNARE complex stability was determined as described previously (Schupp et al., 2016). Briefly,
943 preassembled full-length t-SNARE complexes (WT and mutants, 10 µM) were incubated with the
944 cytoplasmic domain of VAMP2 (30 µM) in 25 mM MOPS (3-(Nmorpholino) propanesulfonic acid)-
945 KOH, pH 7.4, 135 mM KCl, 1% Octyl ß-D-glucopyranoside, 1 mM Dithiothreitol, 10 mM TECEP (Tris(2-
946 carboxyethyl)phosphine hydrochloride)-KOH, pH 7.4, 1 mM EDTA-NaOH, pH 7.4 overnight at 0°C
947 and subsequently for 1 h at 25°C. Subsequently, 37 µl of reaction mixture (36 µg of total protein)
948 was diluted with 213 µl of 1x Laemmli buffer. 7.5 µl aliquots were incubated at the indicated
949 temperatures for 5 min. Samples were analyzed by SDS-PAGE (15% gels) and proteins were
950 visualized by Coomassie brilliant blue staining. Temperature-dependent dissociation of the SNARE
951 complex was quantified by the appearance of free syntaxin-1A (35 kDa protein band released from
952 the high MW SNARE complex) using the Fiji (Image J based) software. Data were normalized to the
953 maximum value of a measurement set.

954 *Silver Staining*

955 Coomassie prestained gels from SDS PAGE were destained overnight in destain solution (30 %
956 methanol, 10 % acetic acid). Gels were gently washed 30 minutes with 10% ethanol and one minute
957 with 0.02% sodium thiosulfate. After short washing with deionized water, gels were stained (0.03%
958 paraformaldehyde, 0.002% silver nitrate) for 15 minutes and again quickly washed with water.
959 Developing solution (0.06% sodium carbonate, 0.018% paraformaldehyde, 0.0002% sodium
960 thiosulfate) was applied to the gels until protein band intensities were satisfactorily stained. The
961 reactions were stopped by replacing the staining solution with 0.07% acetic acid. Gels were scanned
962 and quantified by using the Fiji (Image J based) software.

963 *Statistical analysis*

964 Graphs (bar and line) display mean ± SEM with all points displayed, except when otherwise noted;
965 for electrophysiological experiments *n* denotes the number of cells recorded and is given in the
966 legends. For *in vitro* experiments the number of biological replicates was 3 unless stated otherwise

in the legends. Statistics were performed using GraphPad Prism 9. Unless otherwise noted, statistical differences between several groups were determined by one-way ANOVA; post-test was Dunnett's test comparing to the WT condition as a reference. Equal variance of groups was tested by the Brown-Forsythe test; in case of a significant test, the Brown-Forsythe ANOVA test, which does not assume equal variances, was used instead. Kruskal-Wallis test was used in cases, where the data structure contained many identical values (zeros). Pairwise testing was carried out using unpaired t-test, or Welch's t-test in case of significantly different variances as determined by an F-test. The test is mentioned in the Figure legend; if no test is mentioned, the difference was not significantly different. Significance was assumed when $p<0.05$ and the level of significance is indicated by asterisk: * $p < 0.05$, ** $p < 0.01$, *** $p < 0.001$, **** $p < 0.0001$.

Acknowledgements

We would like to thank Dorte Lauritsen and Ursula Göbel for excellent technical assistance. This investigation was supported by the Novo Nordic Foundation (NNF19OC0058298, JBS), the Independent Research Fund Denmark (8020-00228A, JBS), the Lundbeck Foundation (R277-2018-802, JBS), and the German Reseach Foundation DFG (grant 278001972- TRR 186, THS, JM).

983 **Table 1.**

Mean±SEM	**WT**	**V48F**	**WT**	**D166Y**	***Syt1* WT**	***Syt1* KO**
$\mathbf{k_1}$ [vesicles/s]	385.6 ±52.2	79.87 *** ±12.5	457.4 ±77.4	37.68 **** ±7.33	1227 ±189	646 * ±114
$\mathbf{k_{-1}}$ [1/s]	0.0903 ±0.0091	0.0605 # ±0.011	0.1114 ±0.012	0.0294 **** ±0.0122	0.140 ±0.016	0.114 ¤ ±0.013
$\mathbf{k_f}$ [1/s]	0.000844 ±0.000178	0.0164**** ±0.00230	0.000398 ±0.000077	0.03522**** ±0.00352	0.000235 ±0.000043	0.00286*** ±0.00062

984

985 **Estimated parameters affecting the size of the RRP.** Displayed is mean ±SEM. Two-sample t-test or
986 Welch's t-test comparing mutant to WT: *p<0.05; ***p<0.001; ****p<0.0001, # non-significant
987 (p=0.125), ¤ non-significant (p=0.210).

988 **Literature**

989 Abramov, D., N.G.L. Guiberson, and J. Burre. 2021a. STXBP1 encephalopathies: Clinical spectrum, disease
990 mechanisms, and therapeutic strategies. *J Neurochem*. 157:165-178.
991 Abramov, D., N.G.L. Guiberson, A. Daab, Y. Na, G.A. Petsko, M. Sharma, and J. Burre. 2021b. Targeted
992 stabilization of Munc18-1 function via pharmacological chaperones. *EMBO Mol Med*. 13:e12354.
993 Alten, B., Q. Zhou, O.H. Shin, L. Esquivies, P.Y. Lin, K.I. White, R. Sun, W.K. Chung, L.M. Monteggia, A.T.
994 Brunger, and E.T. Kavalali. 2021. Role of Aberrant Spontaneous Neurotransmission in SNAP25-
995 Associated Encephalopathies. *Neuron*. 109:59-72 e55.
996 Bacaj, T., D. Wu, J. Burre, R.C. Malenka, X. Liu, and T.C. Sudhof. 2015. Synaptotagmin-1 and -7 Are
997 Redundantly Essential for Maintaining the Capacity of the Readily-Releasable Pool of Synaptic
998 Vesicles. *PLoS Biol*. 13:e1002267.
999 Baker, K., S.L. Gordon, H. Melland, F. Bumbak, D.J. Scott, T.J. Jiang, D. Owen, B.J. Turner, S.G. Boyd, M. Rossi,
1000 M. Al-Raqad, O. Elpeleg, D. Peck, G.M.S. Mancini, M. Wilke, M. Zollino, G. Marangi, H. Weigand, I.
1001 Borggraefe, T. Haack, Z. Stark, S. Sadedin, G. Broad Center for Mendelian, T.Y. Tan, Y. Jiang, R.A.
1002 Gibbs, S. Ellingwood, M. Amaral, W. Kelley, M.A. Kurian, M.A. Cousin, and F.L. Raymond. 2018. SYT1-
1003 associated neurodevelopmental disorder: a case series. *Brain*. 141:2576-2591.
1004 Baker, R.W., P.D. Jeffrey, M. Zick, B.P. Phillips, W.T. Wickner, and F.M. Hughson. 2015. A direct role for the
1005 Sec1/Munc18-family protein Vps33 as a template for SNARE assembly. *Science*. 349:1111-1114.
1006 Bao, H., D. Das, N.A. Courtney, Y. Jiang, J.S. Briguglio, X. Lou, D. Roston, Q. Cui, B. Chanda, and E.R. Chapman.
1007 2018. Dynamics and number of trans-SNARE complexes determine nascent fusion pore properties.
1008 *Nature*. 554:260-263.
1009 Basu, J., A. Betz, N. Brose, and C. Rosenmund. 2007. Munc13-1 C1 domain activation lowers the energy
1010 barrier for synaptic vesicle fusion. *J Neurosci*. 27:1200-1210.
1011 Bekkers, J.M., and C.F. Stevens. 1991. Excitatory and inhibitory autaptic currents in isolated hippocampal
1012 neurons maintained in cell culture. *Proc Natl Acad Sci U S A*. 88:7834-7838.
1013 Bouazza-Arostegui, B., M. Camacho, M.M. Brockmann, S. Zobel, and C. Rosenmund. 2022. Deconstructing
1014 Synaptotagmin-1's Distinct Roles in Synaptic Vesicle Priming and Neurotransmitter Release. *J*
1015 *Neurosci*. 42:2856-2871.
1016 Bradberry, M.M., N.A. Courtney, M.J. Dominguez, S.M. Lofquist, A.T. Knox, R.B. Sutton, and E.R. Chapman.
1017 2020. Molecular Basis for Synaptotagmin-1-Associated Neurodevelopmental Disorder. *Neuron*.
1018 107:52-64 e57.
1019 Bronk, P., F. Deak, M.C. Wilson, X. Liu, T.C. Sudhof, and E.T. Kavalali. 2007. Differential effects of SNAP-25
1020 deletion on Ca2+ -dependent and Ca2+ -independent neurotransmission. *J Neurophysiol*. 98:794-
1021 806.
1022 Chang, S., T. Trimbuch, and C. Rosenmund. 2018. Synaptotagmin-1 drives synchronous Ca(2+)-triggered
1023 fusion by C2B-domain-mediated synaptic-vesicle-membrane attachment. *Nat Neurosci*. 21:33-40.
1024 Chen, Y., Y.H. Wang, Y. Zheng, M. Li, B. Wang, Q.W. Wang, C.L. Fu, Y.N. Liu, X. Li, and J. Yao. 2021.
1025 Synaptotagmin-1 interacts with PI(4,5)P2 to initiate synaptic vesicle docking in hippocampal neurons.
1026 *Cell Rep*. 34:108842.
1027 Courtney, K.C., J.D. Vevea, Y. Li, Z. Wu, Z. Zhang, and E.R. Chapman. 2021. Synaptotagmin 1 oligomerization
1028 via the juxtamembrane linker regulates spontaneous and evoked neurotransmitter release. *Proc Natl*
1029 *Acad Sci U S A*. 118.
1030 Courtney, N.A., H. Bao, J.S. Briguglio, and E.R. Chapman. 2019. Synaptotagmin 1 clamps synaptic vesicle
1031 fusion in mammalian neurons independent of complexin. *Nat Commun*. 10:4076.
1032 Das, D., H. Bao, K.C. Courtney, L. Wu, and E.R. Chapman. 2020. Resolving kinetic intermediates during the
1033 regulated assembly and disassembly of fusion pores. *Nat Commun*. 11:231.
1034 Delgado-Martinez, I., R.B. Nehring, and J.B. Sorensen. 2007. Differential abilities of SNAP-25 homologs to
1035 support neuronal function. *J Neurosci*. 27:9380-9391.

1036 Fang, Q., Y. Zhao, A.D. Herbst, B.N. Kim, and M. Lindau. 2015. Positively charged amino acids at the SNAP-25
1037 C terminus determine fusion rates, fusion pore properties, and energetics of tight SNARE complex
1038 zippering. *J Neurosci*. 35:3230-3239.
1039 Fasshauer, D., D. Bruns, B. Shen, R. Jahn, and A.T. Brunger. 1997. A structural change occurs upon binding of
1040 syntaxin to SNAP-25. *J Biol Chem*. 272:4582-4590.
1041 Fasshauer, D., R.B. Sutton, A.T. Brunger, and R. Jahn. 1998. Conserved structural features of the synaptic
1042 fusion complex: SNARE proteins reclassified as Q- and R-SNAREs. *Proc Natl Acad Sci U S A*. 95:15781-
1043 15786.
1044 Fernandez-Busnadiego, R., B. Zuber, U.E. Maurer, M. Cyrklaff, W. Baumeister, and V. Lucic. 2010. Quantitative
1045 analysis of the native presynaptic cytomatrix by cryoelectron tomography. *J Cell Biol*. 188:145-156.
1046 Gao, Y., S. Zorman, G. Gundersen, Z. Xi, L. Ma, G. Sirinakis, J.E. Rothman, and Y. Zhang. 2012. Single
1047 reconstituted neuronal SNARE complexes zipper in three distinct stages. *Science*. 337:1340-1343.
1048 Guiberson, N.G.L., A. Pineda, D. Abramov, P. Kharel, K.E. Carnazza, R.T. Wragg, J.S. Dittman, and J. Burre.
1049 2018. Mechanism-based rescue of Munc18-1 dysfunction in varied encephalopathies by chemical
1050 chaperones. *Nat Commun*. 9:3986.
1051 Hamdan, F.F., C.T. Myers, P. Cossette, P. Lemay, D. Spiegelman, A.D. Laporte, C. Nassif, O. Diallo, J. Monlong,
1052 M. Cadieux-Dion, S. Dobrzeniecka, C. Meloche, K. Retterer, M.T. Cho, J.A. Rosenfeld, W. Bi, C.
1053 Massicotte, M. Miguet, L. Brunga, B.M. Regan, K. Mo, C. Tam, A. Schneider, G. Hollingsworth, S.
1054 Deciphering Developmental Disorders, D.R. FitzPatrick, A. Donaldson, N. Canham, E. Blair, B. Kerr,
1055 A.E. Fry, R.H. Thomas, J. Shelagh, J.A. Hurst, H. Brittain, M. Blyth, R.R. Lebel, E.H. Gerkes, L. Davis-
1056 Keppen, Q. Stein, W.K. Chung, S.J. Dorison, P.J. Benke, E. Fassi, N. Corsten-Janssen, E.J. Kamsteeg,
1057 F.T. Mau-Them, A.L. Bruel, A. Verloes, K. Ounap, M.H. Wojcik, D.V.F. Albert, S. Venkateswaran, T.
1058 Ware, D. Jones, Y.C. Liu, S.S. Mohammad, P. Bizargity, C.A. Bacino, V. Leuzzi, S. Martinelli, B.
1059 Dallapiccola, M. Tartaglia, L. Blumkin, K.J. Wierenga, G. Purcarin, J.J. O'Byrne, S. Stockler, A. Lehman,
1060 B. Keren, M.C. Nougues, C. Mignot, S. Auvin, C. Nava, S.M. Hiatt, M. Bebin, Y. Shao, F. Scaglia, S.R.
1061 Lalani, R.E. Frye, I.T. Jarjour, S. Jacques, R.M. Boucher, E. Riou, M. Srour, L. Carmant, A. Lortie, P.
1062 Major, P. Diadori, F. Dubeau, G. D'Anjou, G. Bourque, S.F. Berkovic, L.G. Sadleir, P.M. Campeau, Z.
1063 Kibar, R.G. Lafreniere, S.L. Girard, S. Mercimek-Mahmutoglu, C. Boelman, et al. 2017. High Rate of
1064 Recurrent De Novo Mutations in Developmental and Epileptic Encephalopathies. *Am J Hum Genet*.
1065 101:664-685.
1066 Hoerder-Suabedissen, A., K.V. Korrell, S. Hayashi, A. Jeans, D.M.O. Ramirez, E. Grant, H.C. Christian, E.T.
1067 Kavalali, M.C. Wilson, and Z. Molnar. 2019. Cell-Specific Loss of SNAP25 from Cortical Projection
1068 Neurons Allows Normal Development but Causes Subsequent Neurodegeneration. *Cereb Cortex*.
1069 29:2148-2159.
1070 Honigmann, A., G. van den Bogaart, E. Iraheta, H.J. Risselada, D. Milovanovic, V. Mueller, S. Mullar, U.
1071 Diederichsen, D. Fasshauer, H. Grubmuller, S.W. Hell, C. Eggeling, K. Kuhnel, and R. Jahn. 2013.
1072 Phosphatidylinositol 4,5-bisphosphate clusters act as molecular beacons for vesicle recruitment. *Nat*
1073 *Struct Mol Biol*. 20:679-686.
1074 Huson, V., M. Meijer, R. Dekker, M. Ter Veer, M. Ruiter, J.R. van Weering, M. Verhage, and L.N. Cornelisse.
1075 2020. Post-tetanic potentiation lowers the energy barrier for synaptic vesicle fusion independently
1076 of Synaptotagmin-1. *Elife*. 9.
1077 Jakhanwal, S., C.T. Lee, H. Urlaub, and R. Jahn. 2017. An activated Q-SNARE/SM protein complex as a possible
1078 intermediate in SNARE assembly. *EMBO J*. 36:1788-1802.
1079 Jiao, J., M. He, S.A. Port, R.W. Baker, Y. Xu, H. Qu, Y. Xiong, Y. Wang, H. Jin, T.J. Eisemann, F.M. Hughson, and
1080 Y. Zhang. 2018. Munc18-1 catalyzes neuronal SNARE assembly by templating SNARE association.
1081 *Elife*. 7.
1082 Jumper, J., R. Evans, A. Pritzel, T. Green, M. Figurnov, O. Ronneberger, K. Tunyasuvunakool, R. Bates, A. Zidek,
1083 A. Potapenko, A. Bridgland, C. Meyer, S.A.A. Kohl, A.J. Ballard, A. Cowie, B. Romera-Paredes, S.
1084 Nikolov, R. Jain, J. Adler, T. Back, S. Petersen, D. Reiman, E. Clancy, M. Zielinski, M. Steinegger, M.
1085 Pacholska, T. Berghammer, S. Bodenstein, D. Silver, O. Vinyals, A.W. Senior, K. Kavukcuoglu, P. Kohli,

1086 and D. Hassabis. 2021. Highly accurate protein structure prediction with AlphaFold. *Nature*. 596:583-
1087 589.
1088 Kalyana Sundaram, R.V., H. Jin, F. Li, T. Shu, J. Coleman, J. Yang, F. Pincet, Y. Zhang, J.E. Rothman, and S.S.
1089 Krishnakumar. 2021. Munc13 binds and recruits SNAP25 to chaperone SNARE complex assembly.
1090 *FEBS Lett*. 595:297-309.
1091 Kedar, G.H., A.S. Munch, J.R. van Weering, J. Malsam, A. Scheutzow, H. de Wit, S. Houy, B. Tawfik, T.H. Sollner,
1092 J.B. Sorensen, and M. Verhage. 2015. A Post-Docking Role of Synaptotagmin 1-C2B Domain Bottom
1093 Residues R398/399 in Mouse Chromaffin Cells. *J Neurosci*. 35:14172-14182.
1094 Kim, J.Y., B.K. Choi, M.G. Choi, S.A. Kim, Y. Lai, Y.K. Shin, and N.K. Lee. 2012. Solution single-vesicle assay
1095 reveals PIP2-mediated sequential actions of synaptotagmin-1 on SNAREs. *EMBO J*. 31:2144-2155.
1096 Klockner, C., H. Sticht, P. Zacher, B. Popp, H.E. Babcock, D.P. Bakker, K. Barwick, M.V. Bonfert, C.G.
1097 Bonnemann, E.H. Brilstra, C. Care4Rare Canada, W.K. Chung, A.J. Clarke, P. Devine, S. Donkervoort,
1098 J.L. Fraser, J. Friedman, A. Gates, J. Ghoumid, E. Hobson, G. Horvath, J. Keller-Ramey, B. Keren, M.A.
1099 Kurian, V. Lee, K.A. Leppig, J. Lundgren, M.T. McDonald, H.M. McLaughlin, A. McTague, H.C. Mefford,
1100 C. Mignot, M.A. Mikati, C. Nava, F.L. Raymond, J.R. Sampson, A. Sanchis-Juan, V. Shashi, J.T.C. Shieh,
1101 M. Shinawi, A. Slavotinek, T. Stodberg, N. Stong, J.A. Sullivan, A.C. Taylor, T.L. Toler, M.J. van den
1102 Boogaard, S.N. van der Crabben, K.L.I. van Gassen, R.H. van Jaarsveld, J. Van Ziffle, A.F. Wadley, M.
1103 Wagner, K. Wigby, S.B. Wortmann, Y.A. Zarate, R.S. Moller, J.R. Lemke, and K. Platzer. 2021. De novo
1104 variants in SNAP25 cause an early-onset developmental and epileptic encephalopathy. *Genet Med*.
1105 23:653-660.
1106 Kovacevic, J., G. Maroteaux, D. Schut, M. Loos, M. Dubey, J. Pitsch, E. Remmelink, B. Koopmans, J. Crowley,
1107 L.N. Cornelisse, P.F. Sullivan, S. Schoch, R.F. Toonen, O. Stiedl, and M. Verhage. 2018. Protein
1108 instability, haploinsufficiency, and cortical hyper-excitability underlie STXBP1 encephalopathy. *Brain*.
1109 141:1350-1374.
1110 Lee, J.S., W.K. Ho, E. Neher, and S.H. Lee. 2013. Superpriming of synaptic vesicles after their recruitment to
1111 the readily releasable pool. *Proc Natl Acad Sci U S A*. 110:15079-15084.
1112 Liu, H., C. Dean, C.P. Arthur, M. Dong, and E.R. Chapman. 2009. Autapses and networks of hippocampal
1113 neurons exhibit distinct synaptic transmission phenotypes in the absence of synaptotagmin I. *J*
1114 *Neurosci*. 29:7395-7403.
1115 Mahal, L.K., S.M. Sequeira, J.M. Gureasko, and T.H. Sollner. 2002. Calcium-independent stimulation of
1116 membrane fusion and SNAREpin formation by synaptotagmin I. *J Cell Biol*. 158:273-282.
1117 Malsam, J., S. Barfuss, T. Trimbuch, F. Zarebidaki, A.F. Sonnen, K. Wild, A. Scheutzow, L. Rohland, M.P. Mayer,
1118 I. Sinning, J.A.G. Briggs, C. Rosenmund, and T.H. Sollner. 2020. Complexin Suppresses Spontaneous
1119 Exocytosis by Capturing the Membrane-Proximal Regions of VAMP2 and SNAP25. *Cell Rep*.
1120 32:107926.
1121 Malsam, J., D. Parisotto, T.A. Bharat, A. Scheutzow, J.M. Krause, J.A. Briggs, and T.H. Sollner. 2012. Complexin
1122 arrests a pool of docked vesicles for fast Ca2+-dependent release. *EMBO J*. 31:3270-3281.
1123 Manca, F., F. Pincet, L. Truskinovsky, J.E. Rothman, L. Foret, and M. Caruel. 2019. SNARE machinery is
1124 optimized for ultrafast fusion. *Proc Natl Acad Sci U S A*. 116:2435-2442.
1125 Martin, S., A. Papadopulos, V.M. Tomatis, E. Sierecki, N.T. Malintan, R.S. Gormal, N. Giles, W.A. Johnston, K.
1126 Alexandrov, Y. Gambin, B.M. Collins, and F.A. Meunier. 2014. Increased polyubiquitination and
1127 proteasomal degradation of a Munc18-1 disease-linked mutant causes temperature-sensitive defect
1128 in exocytosis. *Cell Rep*. 9:206-218.
1129 Mirdita, M., K. Schutze, Y. Moriwaki, L. Heo, S. Ovchinnikov, and M. Steinegger. 2022. ColabFold: making
1130 protein folding accessible to all. *Nat Methods*. 19:679-682.
1131 Mohrmann, R., H. de Wit, M. Verhage, E. Neher, and J.B. Sorensen. 2010. Fast vesicle fusion in living cells
1132 requires at least three SNARE complexes. *Science*. 330:502-505.
1133 Moulder, K.L., and S. Mennerick. 2005. Reluctant vesicles contribute to the total readily releasable pool in
1134 glutamatergic hippocampal neurons. *J Neurosci*. 25:3842-3850.

1135 Naldini, L., U. Blomer, P. Gallay, D. Ory, R. Mulligan, F.H. Gage, I.M. Verma, and D. Trono. 1996. In vivo gene
1136 delivery and stable transduction of nondividing cells by a lentiviral vector. *Science*. 272:263-267.
1137 Neher, E. 2015. Merits and Limitations of Vesicle Pool Models in View of Heterogeneous Populations of
1138 Synaptic Vesicles. *Neuron*. 87:1131-1142.
1139 Parisotto, D., J. Malsam, A. Scheutzow, J.M. Krause, and T.H. Sollner. 2012. SNAREpin assembly by Munc18-
1140 1 requires previous vesicle docking by synaptotagmin 1. *J Biol Chem*. 287:31041-31049.
1141 Parlati, F., T. Weber, J.A. McNew, B. Westermann, T.H. Sollner, and J.E. Rothman. 1999. Rapid and efficient
1142 fusion of phospholipid vesicles by the alpha-helical core of a SNARE complex in the absence of an N-
1143 terminal regulatory domain. *Proc Natl Acad Sci U S A*. 96:12565-12570.
1144 Peng, L., H. Liu, H. Ruan, W.H. Tepp, W.H. Stoothoff, R.H. Brown, E.A. Johnson, W.D. Yao, S.C. Zhang, and M.
1145 Dong. 2013. Cytotoxicity of botulinum neurotoxins reveals a direct role of syntaxin 1 and SNAP-25 in
1146 neuron survival. *Nat Commun*. 4:1472.
1147 Radecke, J., R. Seeger, A. Kadkova, U. Laugks, A. Khosrozadeh, K.N. Goldie, V. Lucic, J.B. Sorensen, and B.
1148 Zuber. 2023. Morphofunctional changes at the active zone during synaptic vesicle exocytosis. *EMBO*
1149 *Rep*:e55719.
1150 Rebane, A.A., B. Wang, L. Ma, H. Qu, J. Coleman, S. Krishnakumar, J.E. Rothman, and Y. Zhang. 2018. Two
1151 Disease-Causing SNAP-25B Mutations Selectively Impair SNARE C-terminal Assembly. *J Mol Biol*.
1152 430:479-490.
1153 Rhee, J.S., L.Y. Li, O.H. Shin, J.C. Rah, J. Rizo, T.C. Sudhof, and C. Rosenmund. 2005. Augmenting
1154 neurotransmitter release by enhancing the apparent Ca2+ affinity of synaptotagmin 1. *Proc Natl Acad*
1155 *Sci U S A*. 102:18664-18669.
1156 Rizo, J. 2022. Molecular Mechanisms Underlying Neurotransmitter Release. *Annu Rev Biophys*. 51:377-408.
1157 Rohena, L., J. Neidich, M. Truitt Cho, K.D. Gonzalez, S. Tang, O. Devinsky, and W.K. Chung. 2013. Mutation in
1158 SNAP25 as a novel genetic cause of epilepsy and intellectual disability. *Rare Dis*. 1:e26314.
1159 Rosenmund, C., and C.F. Stevens. 1996. Definition of the readily releasable pool of vesicles at hippocampal
1160 synapses. *Neuron*. 16:1197-1207.
1161 Ruiter, M., A. Kadkova, A. Scheutzow, J. Malsam, T.H. Sollner, and J.B. Sorensen. 2019. An Electrostatic Energy
1162 Barrier for SNARE-Dependent Spontaneous and Evoked Synaptic Transmission. *Cell Rep*. 26:2340-
1163 2352 e2345.
1164 Saitsu, H., M. Kato, T. Mizuguchi, K. Hamada, H. Osaka, J. Tohyama, K. Uruno, S. Kumada, K. Nishiyama, A.
1165 Nishimura, I. Okada, Y. Yoshimura, S. Hirai, T. Kumada, K. Hayasaka, A. Fukuda, K. Ogata, and N.
1166 Matsumoto. 2008. De novo mutations in the gene encoding STXBP1 (MUNC18-1) cause early infantile
1167 epileptic encephalopathy. *Nat Genet*. 40:782-788.
1168 Santos, T.C., K. Wierda, J.H. Broeke, R.F. Toonen, and M. Verhage. 2017. Early Golgi Abnormalities and
1169 Neurodegeneration upon Loss of Presynaptic Proteins Munc18-1, Syntaxin-1, or SNAP-25. *J Neurosci*.
1170 37:4525-4539.
1171 Schmitz, S.K., J.J. Hjorth, R.M. Joemai, R. Wijntjes, S. Eijgenraam, P. de Bruijn, C. Georgiou, A.P. de Jong, A.
1172 van Ooyen, M. Verhage, L.N. Cornelisse, R.F. Toonen, and W.J. Veldkamp. 2011. Automated analysis
1173 of neuronal morphology, synapse number and synaptic recruitment. *J Neurosci Methods*. 195:185-
1174 193.
1175 Schollmeier, Y., J.M. Krause, S. Kreye, J. Malsam, and T.H. Sollner. 2011. Resolving the function of distinct
1176 Munc18-1/SNARE protein interaction modes in a reconstituted membrane fusion assay. *J Biol Chem*.
1177 286:30582-30590.
1178 Schotten, S., M. Meijer, A.M. Walter, V. Huson, L. Mamer, L. Kalogreades, M. ter Veer, M. Ruiter, N. Brose, C.
1179 Rosenmund, J.B. Sorensen, M. Verhage, and L.N. Cornelisse. 2015. Additive effects on the energy
1180 barrier for synaptic vesicle fusion cause supralinear effects on the vesicle fusion rate. *Elife*. 4:e05531.
1181 Schupp, M., J. Malsam, M. Ruiter, A. Scheutzow, K.D. Wierda, T.H. Sollner, and J.B. Sorensen. 2016.
1182 Interactions Between SNAP-25 and Synaptotagmin-1 Are Involved in Vesicle Priming, Clamping
1183 Spontaneous and Stimulating Evoked Neurotransmission. *J Neurosci*. 36:11865-11880.

1184 Shen, X.M., D. Selcen, J. Brengman, and A.G. Engel. 2014. Mutant SNAP25B causes myasthenia, cortical
1185 hyperexcitability, ataxia, and intellectual disability. *Neurology*. 83:2247-2255.
1186 Shi, L., Q.T. Shen, A. Kiel, J. Wang, H.W. Wang, T.J. Melia, J.E. Rothman, and F. Pincet. 2012. SNARE proteins:
1187 one to fuse and three to keep the nascent fusion pore open. *Science*. 335:1355-1359.
1188 Shu, T., H. Jin, J.E. Rothman, and Y. Zhang. 2020. Munc13-1 MUN domain and Munc18-1 cooperatively
1189 chaperone SNARE assembly through a tetrameric complex. *Proc Natl Acad Sci U S A*. 117:1036-1041.
1190 Sitarska, E., J. Xu, S. Park, X. Liu, B. Quade, K. Stepien, K. Sugita, C.A. Brautigam, S. Sugita, and J. Rizo. 2017.
1191 Autoinhibition of Munc18-1 modulates synaptobrevin binding and helps to enable Munc13-
1192 dependent regulation of membrane fusion. *Elife*. 6.
1193 Sorensen, J.B., K. Wiederhold, E.M. Muller, I. Milosevic, G. Nagy, B.L. de Groot, H. Grubmuller, and D.
1194 Fasshauer. 2006. Sequential N- to C-terminal SNARE complex assembly drives priming and fusion of
1195 secretory vesicles. *EMBO J*. 25:955-966.
1196 Studier, F.W. 2005. Protein production by auto-induction in high density shaking cultures. *Protein Expr Purif*.
1197 41:207-234.
1198 Sudhof, T.C. 2013. Neurotransmitter release: the last millisecond in the life of a synaptic vesicle. *Neuron*.
1199 80:675-690.
1200 Sutton, R.B., D. Fasshauer, R. Jahn, and A.T. Brunger. 1998. Crystal structure of a SNARE complex involved in
1201 synaptic exocytosis at 2.4 A resolution. *Nature*. 395:347-353.
1202 Taschenberger, H., A. Woehler, and E. Neher. 2016. Superpriming of synaptic vesicles as a common basis for
1203 intersynapse variability and modulation of synaptic strength. *Proc Natl Acad Sci U S A*. 113:E4548-
1204 4557.
1205 Verhage, M., and J.B. Sorensen. 2020. SNAREopathies: Diversity in Mechanisms and Symptoms. *Neuron*.
1206 107:22-37.
1207 Vevea, J.D., and E.R. Chapman. 2020. Acute disruption of the synaptic vesicle membrane protein
1208 synaptotagmin 1 using knockoff in mouse hippocampal neurons. *Elife*. 9.
1209 Voleti, R., K. Jaczynska, and J. Rizo. 2020. Ca(2+)-dependent release of synaptotagmin-1 from the SNARE
1210 complex on phosphatidylinositol 4,5-bisphosphate-containing membranes. *Elife*. 9.
1211 Walter, A.M., P.S. Pinheiro, M. Verhage, and J.B. Sorensen. 2013. A sequential vesicle pool model with a single
1212 release sensor and a Ca(2+)-dependent priming catalyst effectively explains Ca(2+)-dependent
1213 properties of neurosecretion. *PLoS Comput Biol*. 9:e1003362.
1214 Wang, S., Y. Li, J. Gong, S. Ye, X. Yang, R. Zhang, and C. Ma. 2019. Munc18 and Munc13 serve as a functional
1215 template to orchestrate neuronal SNARE complex assembly. *Nat Commun*. 10:69.
1216 Washbourne, P., P.M. Thompson, M. Carta, E.T. Costa, J.R. Mathews, G. Lopez-Bendito, Z. Molnar, M.W.
1217 Becher, C.F. Valenzuela, L.D. Partridge, and M.C. Wilson. 2002. Genetic ablation of the t-SNARE SNAP-
1218 25 distinguishes mechanisms of neuroexocytosis. *Nat Neurosci*. 5:19-26.
1219 Weber, J.P., K. Reim, and J.B. Sorensen. 2010. Opposing functions of two sub-domains of the SNARE-complex
1220 in neurotransmission. *EMBO J*. 29:2477-2490.
1221 Weber, T., B.V. Zemelman, J.A. McNew, B. Westermann, M. Gmachl, F. Parlati, T.H. Söllner, and J.E. Rothman.
1222 1998. SNAREpins: minimal machinery for membrane fusion. *Cell*. 92:759-772.
1223 Wierda, K.D., and J.B. Sorensen. 2014. Innervation by a GABAergic neuron depresses spontaneous release in
1224 glutamatergic neurons and unveils the clamping phenotype of synaptotagmin-1. *J Neurosci*. 34:2100-
1225 2110.
1226 Xian, J., S. Parthasarathy, S.M. Ruggiero, G. Balagura, E. Fitch, K. Helbig, J. Gan, S. Ganesan, M.C. Kaufman,
1227 C.A. Ellis, D. Lewis-Smith, P. Galer, K. Cunningham, M. O'Brien, M. Cosico, K. Baker, A. Darling, F. Veiga
1228 de Goes, C.M. El Achkar, J.H. Doering, F. Furia, A. Garcia-Cazorla, E. Gardella, L. Geertjens, C. Klein, A.
1229 Kolesnik-Taylor, H. Lammertse, J. Lee, A. Mackie, M. Misra-Isrie, H. Olson, E. Sexton, B. Sheidley, L.
1230 Smith, L. Sotero, H. Stamberger, S. Syrbe, K.M. Thalwitzer, A. van Berkel, M. van Haelst, C. Yuskaitis,
1231 S. Weckhuysen, B. Prosser, C. Son Rigby, S. Demarest, S. Pierce, Y. Zhang, R.S. Moller, H. Bruining, A.
1232 Poduri, F. Zara, M. Verhage, P. Striano, and I. Helbig. 2022. Assessing the landscape of STXBP1-related
1233 disorders in 534 individuals. *Brain*. 145:1668-1683.

1234 Xu, J., Z.P. Pang, O.H. Shin, and T.C. Sudhof. 2009. Synaptotagmin-1 functions as a Ca2+ sensor for
1235 spontaneous release. *Nat Neurosci*. 12:759-766.
1236 Zhou, Q., Y. Lai, T. Bacaj, M. Zhao, A.Y. Lyubimov, M. Uervirojnangkoorn, O.B. Zeldin, A.S. Brewster, N.K.
1237 Sauter, A.E. Cohen, S.M. Soltis, R. Alonso-Mori, M. Chollet, H.T. Lemke, R.A. Pfuetzner, U.B. Choi, W.I.
1238 Weis, J. Diao, T.C. Sudhof, and A.T. Brunger. 2015. Architecture of the synaptotagmin-SNARE
1239 machinery for neuronal exocytosis. *Nature*. 525:62-67.
1240 Zhou, Q., P. Zhou, A.L. Wang, D. Wu, M. Zhao, T.C. Sudhof, and A.T. Brunger. 2017. The primed SNARE-
1241 complexin-synaptotagmin complex for neuronal exocytosis. *Nature*. 548:420-425.
1242 Zucker, R.S., and W.G. Regehr. 2002. Short-term synaptic plasticity. *Annu Rev Physiol*. 64:355-405.

1243

1244

1245 **Figure Legends**

1246 **Figure 1 – Localization of three pathogenic mutations in SNAP25**
1247 **A** Schematic of the neuronal SNARE complex interacting with C2B domain of synaptotagmin-
1248 1 (Syt1; not to scale) via the primary interface. Position of the I67N mutation in the first SNARE
1249 domain of SNAP25 is depicted by an asterisk.
1250 **B** Interaction site of the C2B domain of Syt1 and SNAP25. Syt1 interacts with SNAP25 both
1251 electrostatically (region I and II) and within the hydrophobic patch (HP patch)(Zhou et al., 2015).
1252 **C** Position of the disease-linked mutations V48F (hydrophobic patch) and D166Y (region I) in
1253 the SNARE complex.
1254
1255 **Figure 2** – **Pathogenic SNAP25 mutations compromise neuronal viability, but not synaptogenesis**
1256 **A** SNAP25 V48F and D166Y mutations are similarly expressed as the WT SNAP25 protein.
1257 EGFP-SNAP25 was overexpressed in neurons from CD1 (wildtype) mice; both endogenous and
1258 overexpressed SNAP25 are shown. Valosin-containing protein (VCP) was used as loading control.
1259 **B** Representative images of control (WT) and mutant (V48F, D166Y) hippocampal neurons
1260 stained by dendritic (MAP2) and synaptic (vGlut1) markers. Displayed is MAP2 staining, representing
1261 the cell morphology, in inserts MAP2 staining is depicted in red and vGlut staining in cyan. The scale
1262 bar represents 50 µm.
1263 **C** Number of synapses per neuron in WT and mutant cells.
1264 **D** Total dendritic length of WT and mutant neurons.
1265 **E** Cell viability represented as the number of neurons per glia island. ****p <0.0001, **p
1266 <0.01, *p<0.05, Brown-Forsythe ANOVA test with Dunnett's multiple comparisons test.
1267
1268 **Figure 3 –V48F and D166Y mutations increase miniature EPSC frequency**
1269 **A,D,G** Example traces of mEPSC release for WT, mutant and 1:1 co-expression of WT and mutant
1270 SNAP25, or (**G**) Syt1 WT and KO.
1271 **B, E** The mEPSC frequencies were increased in both V48F and D166Y mutants and co-expressed
1272 conditions (V48F: n = 49, 47, 48 for WT, coexpressed and mutant conditions, respectively; D166Y: n
1273 = 54, 43, 50). ****p <0.0001, ***p <0.001, Brown-Forsythe ANOVA test with Dunnett's multiple
1274 comparisons test.
1275 **C, F** mEPSC amplitudes were on average increased by the V48F and D166Y mutations; this was
1276 significant for the V48F. *p <0.05, ANOVA with Dunnett's multiple comparison test.
1277 **H, I** Syt1 WT and KO data (Syt1: n = 28, 26 for the WT and KO condition). The mEPSC frequencies
1278 and amplitudes were increased and decreased in the KO, respectively. ****p <0.0001, Welch's t-
1279 test, *p<0.05, unpaired t-test.
1280
1281 **Figure 4 – V48F and D166Y mutations reduce the amplitude of the EPSC**
1282 **A, E, I** Example evoked excitatory post-synaptic currents (eEPSC) for WT, SNAP25 mutants and co-
1283 expressed WT/mutants, or (**I**) Syt1 WT and KO.
1284 **B, F, J** EPSC amplitude was decreased by both SNAP25 mutations (V48F: n = 50, 50, 45 for WT, co-
1285 expressed and mutant conditions, respectively; D166Y: n = 56, 35, 44) and by Syt1 KO (Syt1: n = 19,

26 for the WT and KO condition). SNAP25 mutations: ****p <0.0001, **p <0.01, Brown-Forsythe ANOVA test with Dunnett's multiple comparisons test; Syt1: ****p<0.0001, Welch's t-test.

C, G, K Overall evoked charge after a single depolarization (V48F: n = 50, 45, 50 for WT, mutant and co-expressed conditions, respectively; D166Y: 56, 44, 35; Syt1: 19, 20 for WT and KO). SNAP25: *p <0.05, Brown-Forsythe ANOVA with Dunnett's multiple comparison test; Syt1: ****p<0.0001, Welch's t-test.

D, H, L Fractional contribution of the synchronous release component to the overall charge (V48F: n = 50, 50, 45 for WT, co-expressed and mutant conditions, respectively; D166Y: 56, 35, 44; Syt1: 19, 20 for WT and KO). SNAP25: ****p <0.0001, ***p <0.001, Brown-Forsythe ANOVA (V48F) or standard ANOVA (D166Y) with Dunnett's multiple comparisons test; Syt1: ****p<0.0001, Welch's t-test.

Figure 5 – The apparent energy barrier for vesicle fusion is lowered by V48F and D166Y, but not by removing Syt1.

A, F, K Example traces for the WT, mutant and co-expressed condition. Each cell was stimulated by 0.25 M (in grey) and 0.5 M sucrose (in black or color).

B, G, L The charge released by 0.25 M sucrose (V48F: n = 28, 30, 29 for WT, co-expressed and mutant conditions, respectively; D166Y: n = 33, 30, 35; Syt1: n = 23, 18 for WT and KO). Syt1: p<0.05, Welch's t-test.

C, H, M The charge released by 0.5 M sucrose (V48F: n = 28, 30, 29 for WT, co-expressed and mutant conditions, respectively; D166Y: n = 33, 30, 35; Syt1: n = 23, 26 for WT and KO). SNAP25: ****p <0.0001, **p <0.01, *p<0.05, Brown-Forsythe ANOVA with Dunnett's multiple comparisons test; Syt1: p=0.0548, unpaired t-test.

D, I, N The ratio of 0.25 and 0.5 M sucrose pool (V48F: n = 28, 30, 29 for WT, co-expressed and mutant conditions, respectively; D166Y: n = 33, 30, 35; Syt1: n = 23, 18 for WT and KO). SNAP25: ****p <0.0001, **p <0.01, ANOVA with Dunnett's multiple comparisons test; Syt1: *p < 0.05, unpaired t-test.

E, J, O Release probability calculated by dividing the charge of an eEPSC with the 0.5 M sucrose pool (V48F: n = 24, 25, 22 for WT, co-expressed and mutant conditions, respectively; D166Y: n = 33, 24, 30; Syt1, n = 16, 21 for WT and KO). SNAP25: ***p <0.001, ANOVA with Dunnett's multiple comparisons test; Syt1: ****p<0.0001, unpaired t-test.

Figure 6 – Dissection of the RRP reduction in V48F and D166Y mutations.

A One-pool model of the Readily Releasable Pool (RRP). k_1 is the rate of priming (units vesicles/s), k_{-1} is the rate of depriming (s^{-1}), k_f is the rate of fusion (s^{-1}).

B Estimation of the three parameters from the response to 0.5 M sucrose and a measurement of the spontaneous release rate.

C Variance-mean analysis in 50 ms intervals during the sucrose application allows determination of the corrected baseline by back-extrapolation of a regression line to the variance of the baseline.

D Normalized mEPSC frequency (k_f) for V48F, D166Y and Syt1 KO. (V48F: n = 23, 24 for WT and mutant conditions, respectively; D166Y: n = 19, 19; Syt1: n = 23, 26). Brown-Forsythe ANOVA

test with Dunnett's multiple comparison test, testing the three mutant conditions against each other. ****p <0.0001, ***p <0.001.

E Normalized RRP size for WT and mutant conditions, with indications of the effect of the mutant-induced changes in k_1, k_{-1}, and k_f on the RRP size.

Figure 7 – SNAP25 V48F and D166Y mutations change short-term plasticity towards facilitation.

A, E EPSCs in response to 50 APs at 40 Hz recorded in 4 mM extracellular Ca^{2+} (V48F: 27, 17, 15 for WT, co-expressed and mutant conditions, respectively; D166Y: 27, 18, 16). Inserts: Normalized EPSC amplitudes demonstrating facilitation of mutant conditions. ****p<0.0001; **p<0.01, Brown-Forsythe ANOVA with Dunnett's multiple comparison test.

B, F Priming rate calculated as the slope of a linear fit to the cumulative evoked charges during the last part of stimulation (V48F: 27, 17, 15 for WT, co-expressed and mutant conditions, respectively; D166Y: 27, 18, 16). *p <0.05, ANOVA (V48F) or Brown-Forsythe ANOVA (D166Y) with Dunnett's multiple comparisons test.

C, G RRP calculated by back-extrapolation of a linear fit to the cumulative evoked charges during the last part of stimulation (V48F: 27, 17, 15 for WT, co-expressed and mutant conditions, respectively; D166Y: 27, 18, 16). **p <0.01, *p <0.05, ANOVA (V48F) or Brown-Forsythe ANOVA (D166Y) with Dunnett's multiple comparisons test.

D, H Release probability calculated as the charge of the first evoked response divided by the RRP obtained by back-extrapolation (V48F: 27, 17, 15 for WT, co-expressed and mutant conditions, respectively; D166Y: 27, 18, 16). ***p<0.001; **p <0.01, ANOVA (V48F) or Brown-Forsythe ANOVA (D166Y) with Dunnett's multiple comparisons test.

Figure 8 – Pathogenic SNAP25 mutations affect synaptotagmin-1 interaction and fusion rates *in vitro*.

A In the presence of SDS, SNAP25 I67N containing v-/t-SNARE complexes were more sensitive to temperature-dependent dissociation. Shown are mean ± SEM (n = 3) for SNARE-complexes including SNAP25 WT and the I67N, V48F and D166Y mutations.

B-C *In vitro* Syt1/VAMP2 SUVs docking to t-SNARE GUVs was significantly reduced by SNAP25 V48F, I67N and D166Y mutants either in absence (**B**) or presence (**C**) of $PI(4,5)P_2$. Fusion was blocked by performing the assay on ice.

D-E *In vitro* lipid mixing assays of VAMP/Syt1 SUVs with t-SNARE GUVs containing SNAP25 V48F, I67N, or D166Y mutants showed impaired membrane fusion in the absence (left) or presence (right) of complexin-II. Fusion clamping in the presence of complexin was selectively reduced by V48F and D166Y. Bar diagrams show lipid mixing just before (pre) and after (post) Ca^{2+} addition and at the end of the reaction. Shown is mean ± SEM (n = 3).

Figure 9 – The D166Y mutation increases binding to its SNARE partners.

A-C *In vitro* lipid mixing assays of VAMP/Syt1 SUVs with syntaxin-1A GUVs in the presence of soluble SNAP25. V48F, and D166Y mutants showed impaired fusion clamping in the absence (left) or presence (right) of complexin-II; I67N (red) showed impaired Ca^{2+}-independent and Ca^{2+}-

1369 triggered fusion. Bar diagrams show lipid mixing just before (pre) and after (post) Ca^{2+} addition and
1370 at the end of the reaction. Mean ± SEM (n = 3).
1371 **D** SNAP25 D166Y showed enhanced interactions with SUVS carrying reconstituted syntaxin-
1372 1A (Stx-1), VAMP2, Syt1/VAMP2 or a SUV-mixture containing Syntaxin-1A and VAMP2/Syt1 in co-
1373 flotation assays, whereas V48F displayed weaker increases in interactions with SUVs containing
1374 syntaxin-1A, or Syt1/VAMP2. Shown is mean ± SEM on a logarithmic scale. *** p<0.001, ** p<0.01,
1375 * p<0.05, two-tailed one-sample t-test comparing to 1.
1376
1377 **Figure 10 – The I67N mutation inhibits spontaneous and evoked release.**
1378 **A** SNAP25 I67N is similarly expressed as the WT SNAP25 protein. EGFP-SNAP25 was
1379 overexpressed in neurons from CD1 (wildtype) mice; both endogenous and overexpressed SNAP25
1380 are shown. Valosin-containing protein (VCP) was used as the loading control.
1381 **B** Representative image of mutant (I67N) hippocampal neurons stained for the dendritic
1382 marker MAP2 and the synaptic markers vGlut1. Displayed is MAP2 staining, representing the cell
1383 morphology, in inserts MAP2 staining is depicted in red and vGlut staining in cyan. The scale bar
1384 represents 50 µm.
1385 **C** Cell viability represented as the number of neurons per glial islet. ****p <0.0001, Brown-
1386 Forsythe ANOVA test with Dunnett's multiple comparisons test.
1387 **D** Number of synapses per neuron in WT and mutant cells. The WT data are the same as in
1388 Fig. 2B because these experiments were carried out in parallel. The difference was tested using
1389 ANOVA between all conditions, which was non-significant.
1390 **E** Total dendritic length of WT and mutant neurons.
1391 **F** Example traces of mEPSC release for WT, mutant (I67N) and 1:1 co-expression of WT and
1392 SNAP25 mutant.
1393 **G** The mini frequency was decreased in both I67N mutant and the WT+I67N combination
1394 (I67N: n = 39, 36, 30 for WT, coexpressed and mutant). ****p <0.0001, ***p <0.001, Kruskal-Wallis
1395 with Dunn's multiple comparisons.
1396 **H** mEPSC amplitudes were unchanged by the I67N mutation.
1397 **I** Example evoked excitatory post-synaptic currents (eEPSC) for WT, mutant (I67N) and co-
1398 expressed WT and mutant.
1399 **J** EPSC amplitude was decreased by the I67N mutations (I67N: n = 39, 37, 30 for WT, co-
1400 expressed and mutant conditions, respectively). SNAP25 mutations: ****p <0.0001, **p <0.01,
1401 Brown-Forsythe ANOVA test with Dunnett's multiple comparisons test.
1402 **K** Overall evoked charge after a single depolarization (I67N: 24, 10, 0 for WT, co-expressed
1403 and mutant conditions, respectively).
1404 **L** Fractional contribution of the synchronous release component to the overall charge (I67N:
1405 24, 10, 0 for WT, co-expressed and mutant conditions, respectively).
1406
1407 **Figure 11 – The I67N mutation has normal RRP size, but increased energy barrier for fusion.**
1408 **A, E** Example traces for the WT, mutant and co-expressed condition. Each cell was stimulated
1409 by 0.25 M (**A**, in grey) and 0.5 M sucrose (**A**, in color) or 0.375 M sucrose (**E**, in grey) and 0.75 M (**E**,
1410 in color).

1411 **B, F** The charge released by 0.25 M sucrose (**B**, I67N: n = 21, 15, 8 for WT, co-expressed and
1412 mutant conditions, respectively) or 0.375 M sucrose (**F**, I67N: n = 12, 16, 18; a few cells were
1413 stimulated with 0.35 M sucrose – shown with open symbols). **B**, **p<0.01; *p<0.05, Kruskal-Wallis
1414 test with Dunn's multiple comparison test; **F**, p=0.0339 Brown Forsythe ANOVA test; Dunnett's
1415 multiple comparison test, p=0.0571.
1416 **C, G** The charge released by 0.5 M sucrose (**C**, I67N: n = 21, 15, 8 for WT, co-expressed and
1417 mutant conditions, respectively), or 0.75 M sucrose (**G**, I67N: n = 13, 16, 18). **C**, **p<0.01, *p<0.05,
1418 Brown-Forsythe ANOVA with Dunnett's multiple comparisons test.
1419 **D, H** The ratio of the 0.25 and 0.5 M sucrose pool (**D**, I67N: n = 21, 15, 8 for WT, coexpressed
1420 and mutant conditions, respectively), or the ratio of 0.375 and 0.75 M sucrose pool (**H**, n = 13, 16,
1421 18). **D**, * p<0.05, Kruskal-Wallis test with Dunn's multiple comparisons test. **H**, **** p<0.0001; ***
1422 p<0.001, ANOVA with Dunnett's multiple comparisons test.
1423 **I** EPSCs in response to 50 APs at 40 Hz recorded in 2 mM extracellular Ca^{2+} (I67N: n = 23, 16,
1424 20 for WT, co-expressed and mutant conditions, respectively). Inserts: Normalized EPSC amplitudes
1425 demonstrating facilitation of mutant conditions.
1426 **J** Normalized EPSC amplitudes in response to 50 APs at 40 Hz recorded in 2 mM extracellular
1427 Ca^{2+}.
1428 **K** Paired pulse ratio at interstimulus interval 25 ms (I67N: n = 24, 14, 17 for WT, co-expressed
1429 and mutant conditions, respectively). *p<0.05, ANOVA with Dunnett's multiple comparison test.
1430

1431 **Figure 12 - Adding positive surface charges to the SNARE complex partly compensate for the I67N**
1432 **mutation.**
1433 **A** Example traces of mEPSC release for WT, I67N/E183K/S187K/T190K/E194K ('I67N/4K') and
1434 E183K/S187K/T190K/E194K ('4K') SNAP25. Data from the 4K mutation was obtained in a separate
1435 experiment and is shown for comparison, but statistical tests with 4K mutation data were not
1436 carried out.
1437 **B** The mini frequencies for the WT and I67N/4K are not significantly different; data from the
1438 4K mutation is shown for comparison (n = 19, 25, 13 for WT, I67N/4K and 4K, respectively).
1439 **C** Mini amplitudes remain unaffected by I67N/4K mutation.
1440 **D-E** eEPSC examples (**D**) and amplitudes (**E**) for WT and I67N/4K; 4K is shown for comparison (n
1441 = 19, 25, 13 for WT, I67N/4K and 4K, respectively). ****p<0.0001 Mann-Whitney test.
1442 **F** Electrostatic triggering model (blue line; Ruiter et al., 2019) refitted to WT spontaneous
1443 and evoked data points (black points). Fitted parameters: rate 0.00029 s^{-1} at zero (0) charge (Z);
1444 fraction f=0.030; the maximum rate was fixed at 6000 s^{-1}. WT (black points), I67N, I67N/4K (red
1445 points): means of log-transformed data. The charge-values (Z, horizontal axis) for I67N and I67N/4K
1446 were found by interpolation in the model; the two spontaneous points (I67N, I67N/4K) are
1447 separated by 5.6 charges. For evoked release, rates were found by deconvolution and normalizing
1448 to $RRP_{0.5}$ (Ruiter et al., 2019). The Z-values for evoked release were found by interpolation in the
1449 model; the two mutants (I67N, I67N/4K) are separated by 5.9 charges.
1450

1451 **Figure 13 – Energy landscapes.**
1452 The energy landscapes of WT and mutants were calculated as explained in Materials and Methods
1453 and displayed to scale. Energy landscapes for D166Y (**A**), V48F (**B**) and *Syt1* KO (**C**) are shown at rest
1454 and are characterized by a higher priming barrier ("loss-of-function" phenotype), a destabilized RRP

1455 and a lower fusion barrier ("gain-of-function" phenotype). The I67N (**D**) is characterized by a higher
1456 fusion barrier ("loss-of-function" phenotype). The relative increase in the fusion barrier by the I67N
1457 mutation is higher during stimulation than at rest. Dotted lines represent energy levels for which
1458 less is known.
1459
1460 **Figure 4 – Figure Supplement 1. Kinetic parameters of evoked EPSCs.**
1461 **A** eEPSC (black trace), and integrated eEPSC (after multiplication with -1, red trace) with
1462 double exponential fit (green trace).
1463 **B** Zoom-in of eEPSC (black trace), and integrated EPSC (after multiplication with -1, red trace)
1464 with double exponential fit (green trace). Equations for integration and double exponential function
1465 used for fit is given.
1466
1467 **Figure 4 – Figure Supplement 2. Kinetic parameters of evoked EPSCs.**
1468 **A, E, I** Synchronous release components (**A**, V48F: n = 50, 50, 45 for WT, co-expressed and mutant
1469 conditions, respectively; **E**, D166Y: n = 56, 35, 44; **I**, *Syt1*: 19, 20 for WT and KO). **A**: * $p < 0.05$, Welch's
1470 ANOVA with Dunnett's multiple comparison test, **E**: *** $p < 0.001$, Brown-Forsythe ANOVA with
1471 Dunnett's multiple comparison test, **I**: **** $p < 0.0001$, Welch's unpaired t-test.
1472 **B, F, J** Asynchronous release components. **B**: ** $p < 0.01$; * $p < 0.05$, Brown-Forsythe ANOVA with
1473 Dunnett's multiple comparison test.
1474 **C, G, K** Fast time constants. **C**: **** $p < 0.0001$; ** $p < 0.01$, Brown-Forsythe ANOVA with Dunnett's
1475 multiple comparison test, **G**: **** $p < 0.0001$, Brown-Forsythe ANOVA with Dunnett's multiple
1476 comparison test, **K**: **** $p < 0.0001$, Welch's unpaired t-test.
1477 **D, H, L** Slow time constants.
1478
1479 **Figure 6 – Figure Supplement 1. Effect of sucrose stimulation on estimates of k_1 and k_{-1}.**
1480 The figure shows the effect of the fold-increase in fusion rate (*N*) induced by sucrose (abscissa) on
1481 the estimates of k_1 (**A**, **C**) or k_{-1} (**B, D**) using Eqs. 3, 4 and 5b and the values estimated for D166Y (**A**,
1482 **B**), V48F (**C**, **D**) and WT (Table 1). Previous data showed that 0.5 M sucrose increases the fusion rate
1483 by a factor ~5000 (Schotten et al., 2015). The plots show that the estimates in Table 1 are not strongly
1484 affected by small changes in the effect of sucrose upon k_f.
1485
1486 **Figure 7 – Figure Supplement 1. Train stimulations of V48F and D166Y in 2 mM Ca^{2+}.**
1487 **A, D** EPSCs in response to 50 APs at 40 Hz recorded in 2 mM extracellular Ca^{2+} (V48F: 25, 18, 24
1488 for WT, co-expressed and mutant conditions, respectively; D166Y: 23, 15, 15). Inserts: Normalized
1489 EPSC amplitudes of first five stimulations. * $p < 0.05$, *** $p < 0.001$, one-way ANOVA with Dunnett's
1490 multiple comparison test.
1491 **B, E** Priming rate calculated by as the slope of a linear fit to the cumulative evoked charges
1492 during the last part of stimulation (V48F: 24, 18, 24 for WT, co-expressed and mutant conditions,
1493 respectively; D166Y: 23, 15, 15).
1494 **C, F** RRP calculated by back-extrapolation of a linear fit to the cumulative evoked charges during
1495 the last part of stimulation (V48F: 24, 18, 24 for WT, co-expressed and mutant conditions,
1496 respectively; D166Y: 23, 15, 15).

1497

1498 **Figure 7 – Figure Supplement 2. Cumulative charges of V48F and D166Y trains in 4 mM Ca^{2+}.**
1499 **A, B** Cumulative charges obtained by integrating EPSCs during 40 Hz trains. The slope of the
1500 linear part of the curve reports on the priming rate, which is reduced by the mutations. The back
1501 extrapolation of the linear fit to zero time reports on the RRP_{ev}, the part of the RRP which APs draw
1502 on, which is also reduced by mutation (V48F: n= 27, 17, 15 for WT, co-expressed and mutant
1503 conditions, respectively; D166Y: 27, 18, 16).

1504 **Figure 9 – Figure Supplement 1. Floatation assay.**
1505 Example Coomassie and silver stained gels demonstrating binding of SNAP25 WT and mutants to
1506 different populations of SUVs: Syntaxin-1 (Stx-1) and VAMP2/Syt1, Syntaxin-1 (Stx-1), VAMP2/Syt1,
1507 VAMP2, or Syt1 SUVs. Note increased binding of D166Y and V48F to most SUV populations, strongest
1508 for D166Y (quantified data in Fig. 9D).
1509

1510 **Figure 9 – Figure Supplement 2. AlphaFold prediction of mutants.**
1511 The figure shows an overlay of the WT protein and the three mutants I67N, V48F and D166Y as
1512 predicted by AlphaFold (Jumper et al., 2021; Mirdita et al., 2022). No major structural changes were
1513 detected, but V48F is expected to alter the interaction with neighboring E52, whereas D166Y will
1514 induce a stronger interaction with H162.

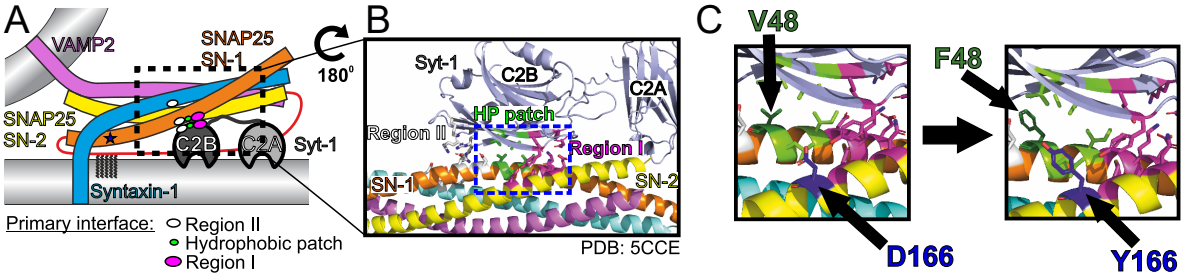

Kádková et al., Fig. 1

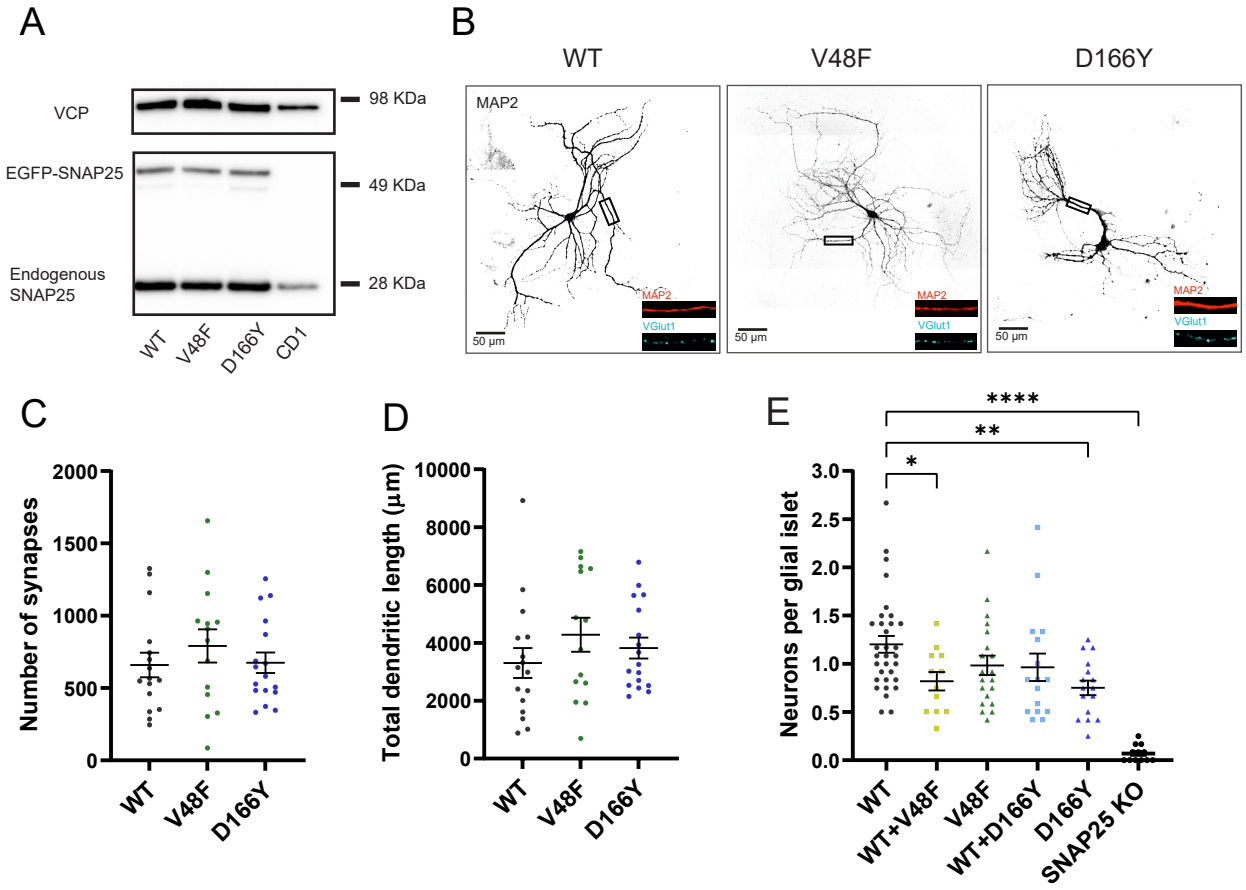

Kádková et al., Fig. 2

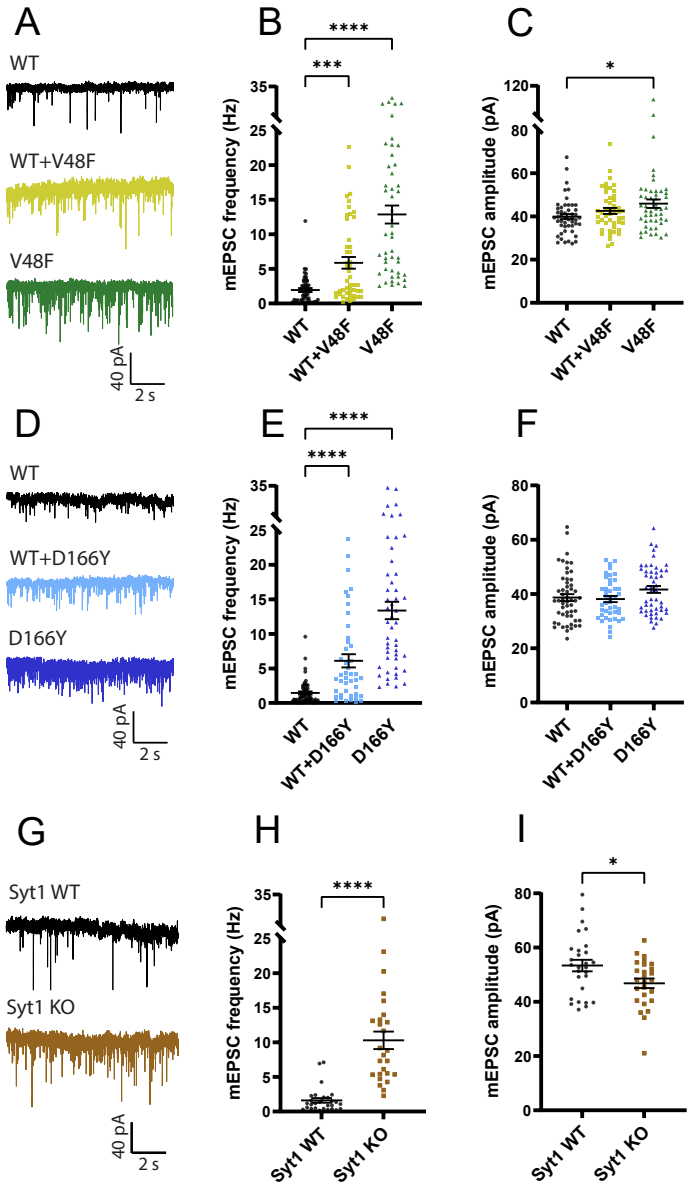

Kádková et al., Fig. 3

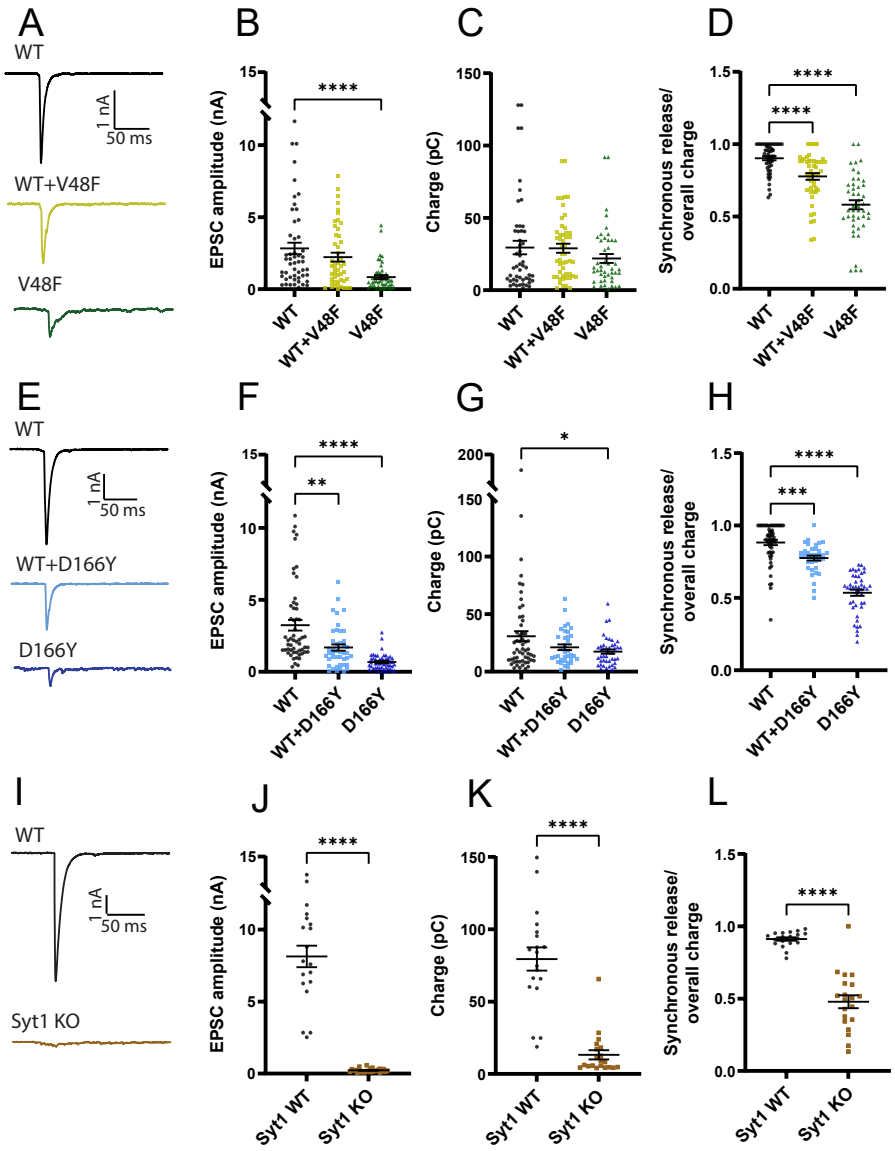

Kádková et al., Fig. 4

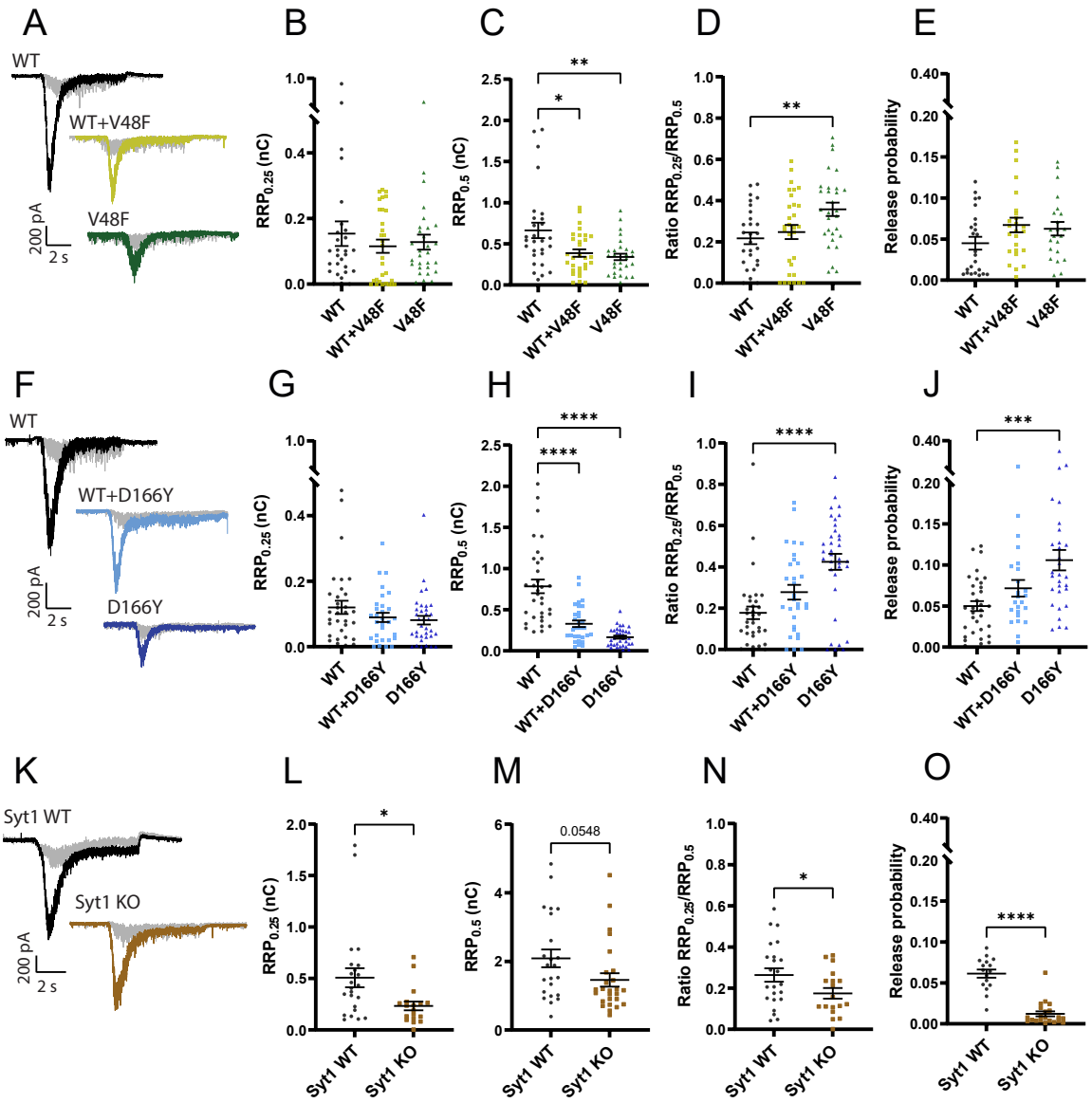

Kádková et al., Fig. 5

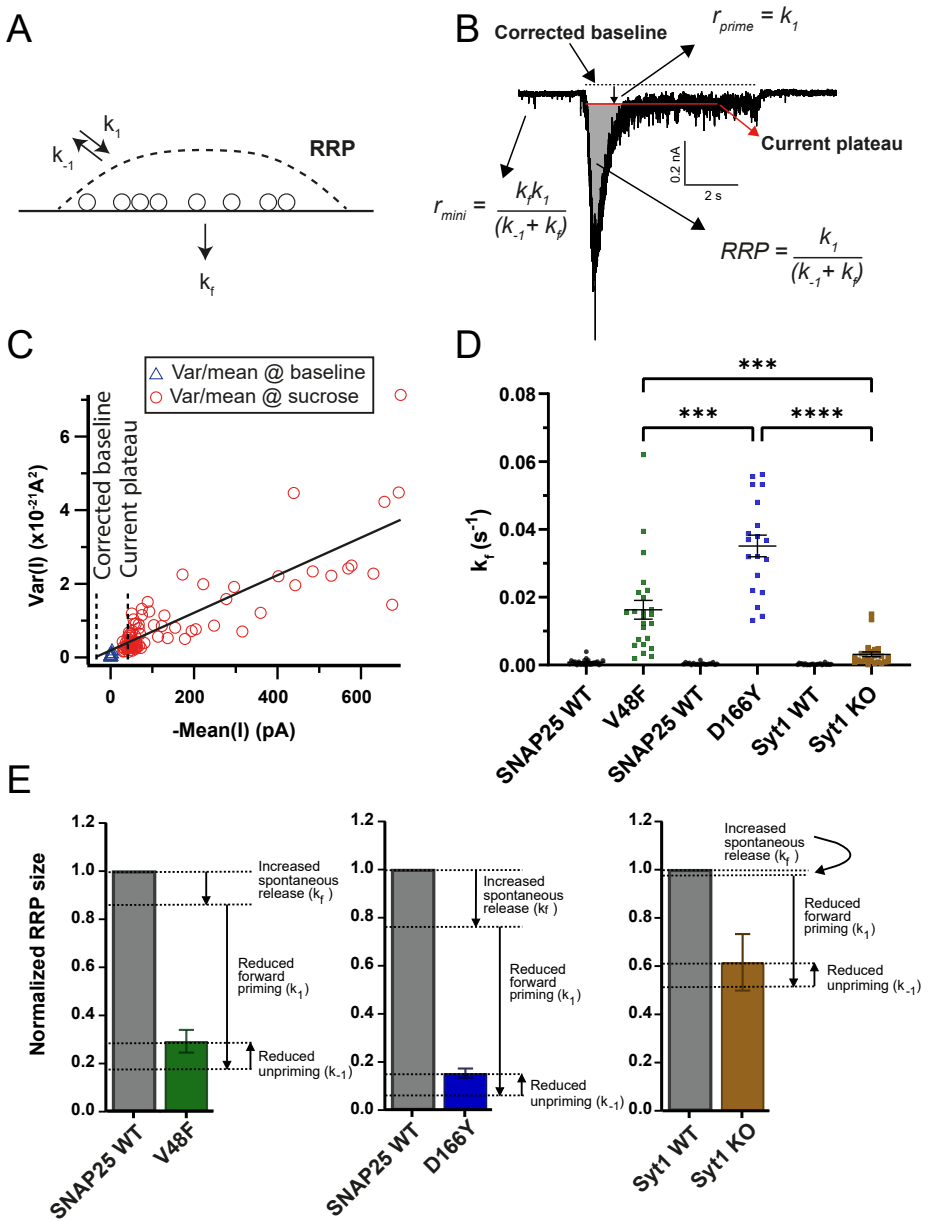

Kádková et al., Fig. 6

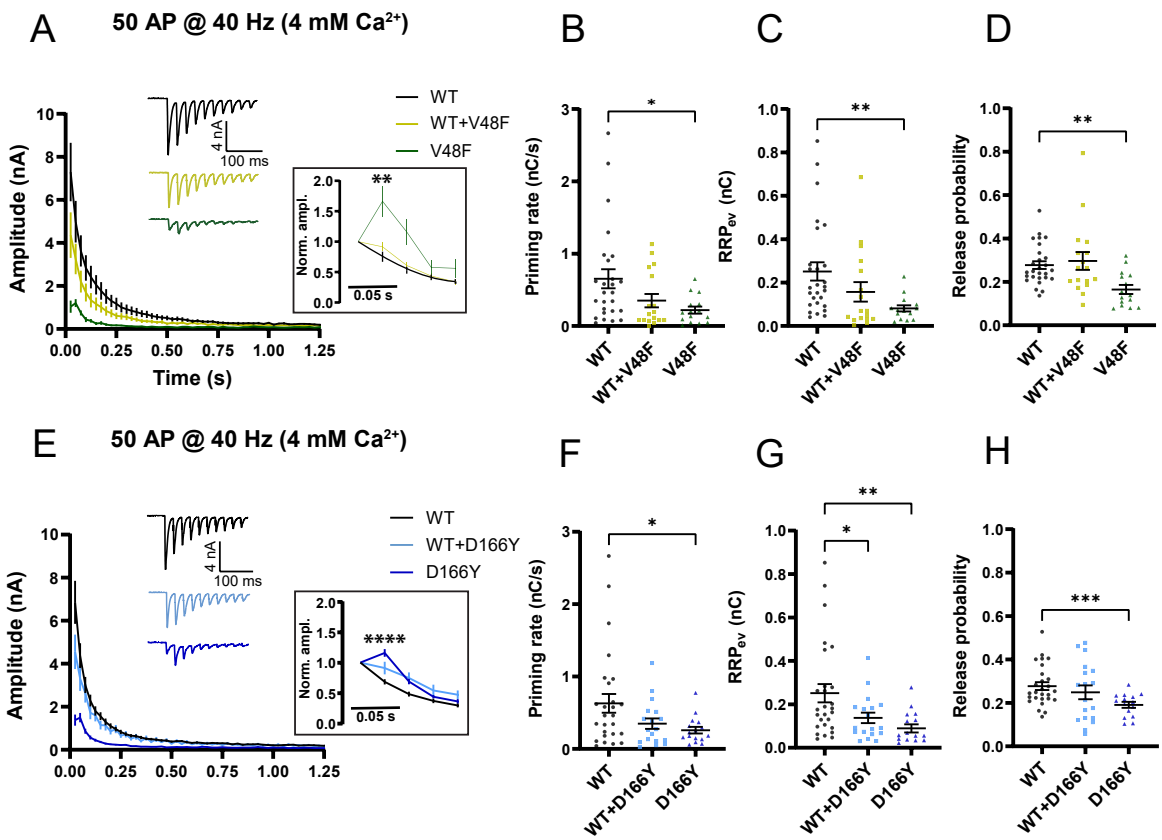

Kádková et al., Fig. 7

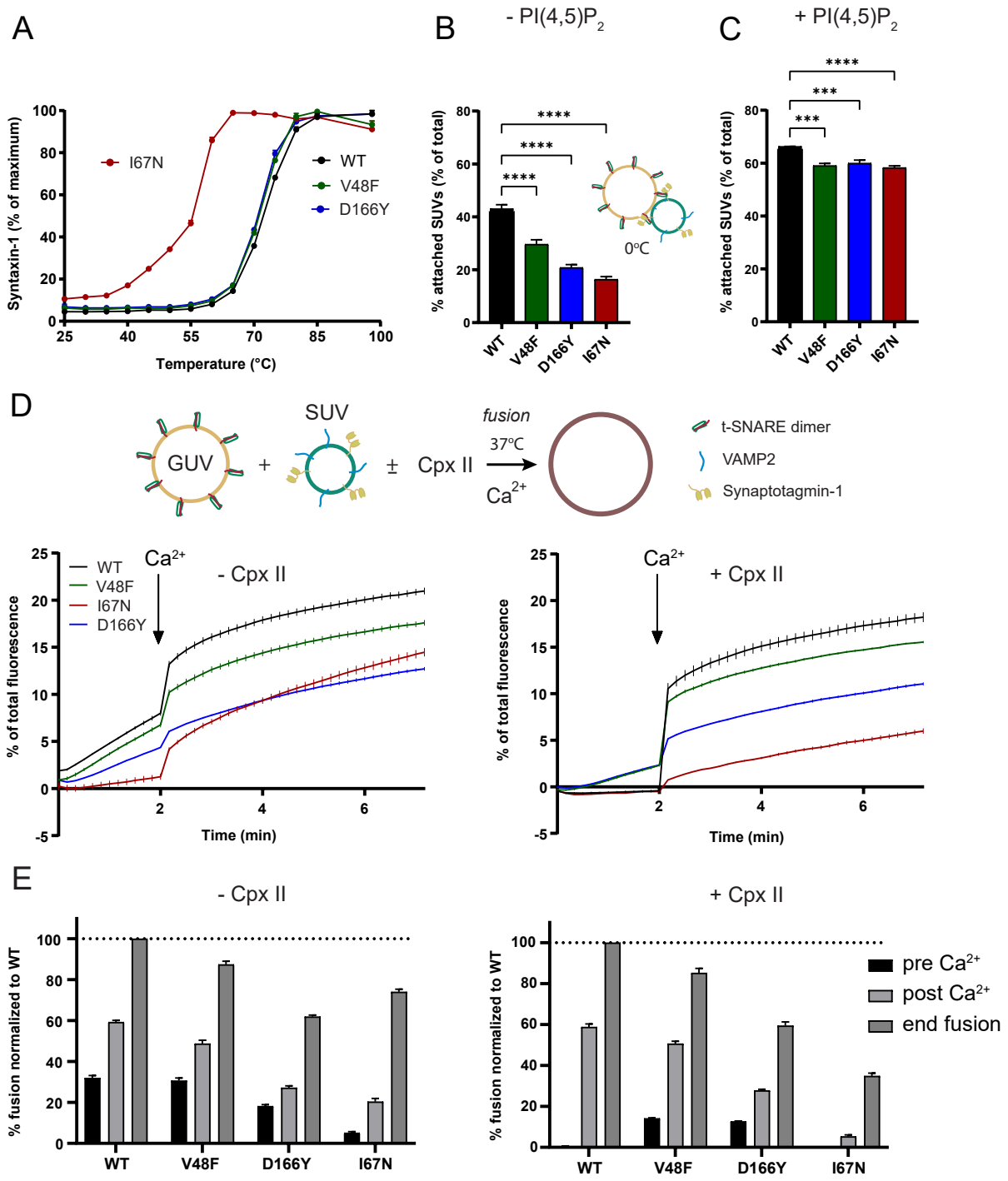

Kádková et al., Fig. 8

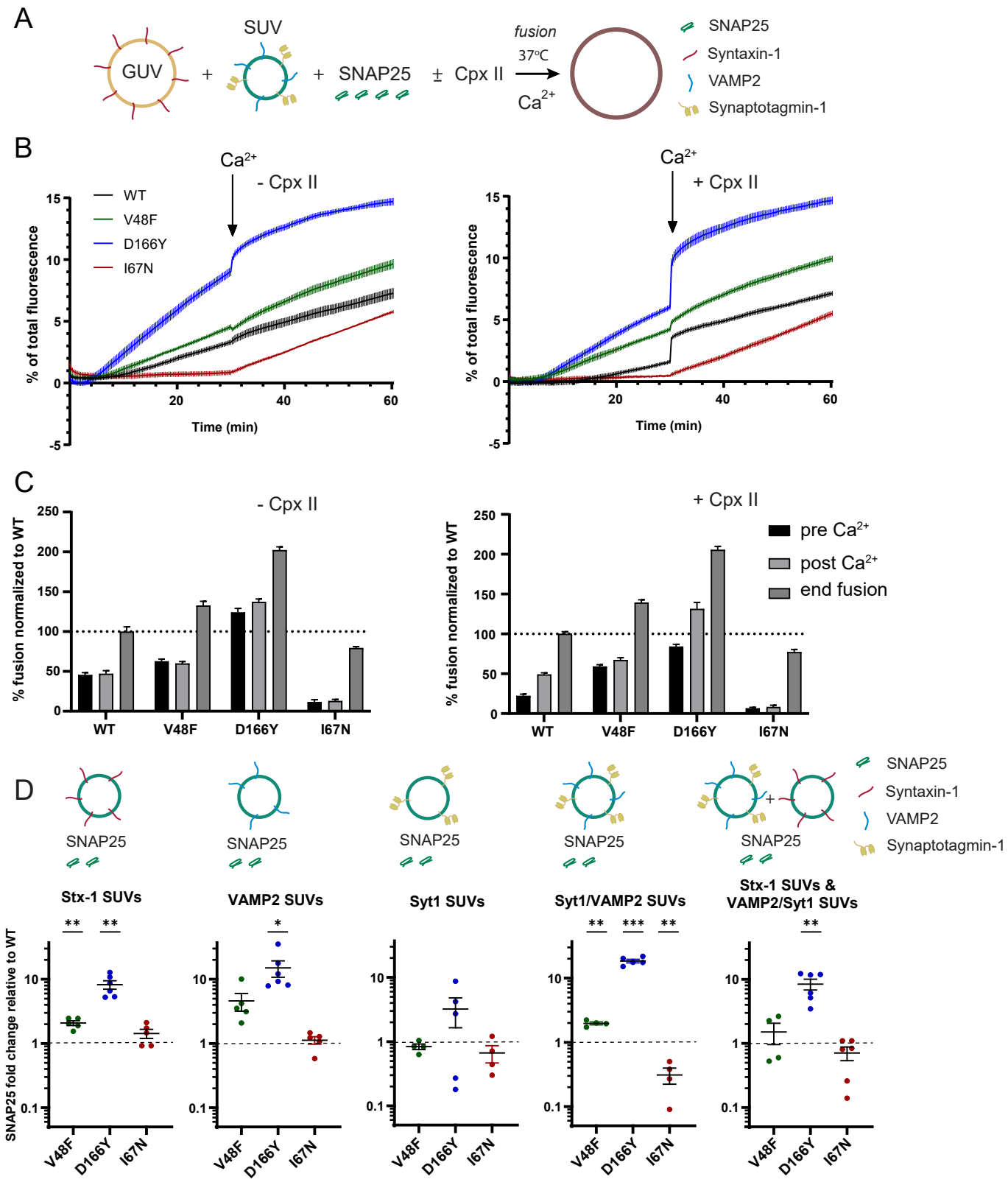

Kádková et al., Fig. 9

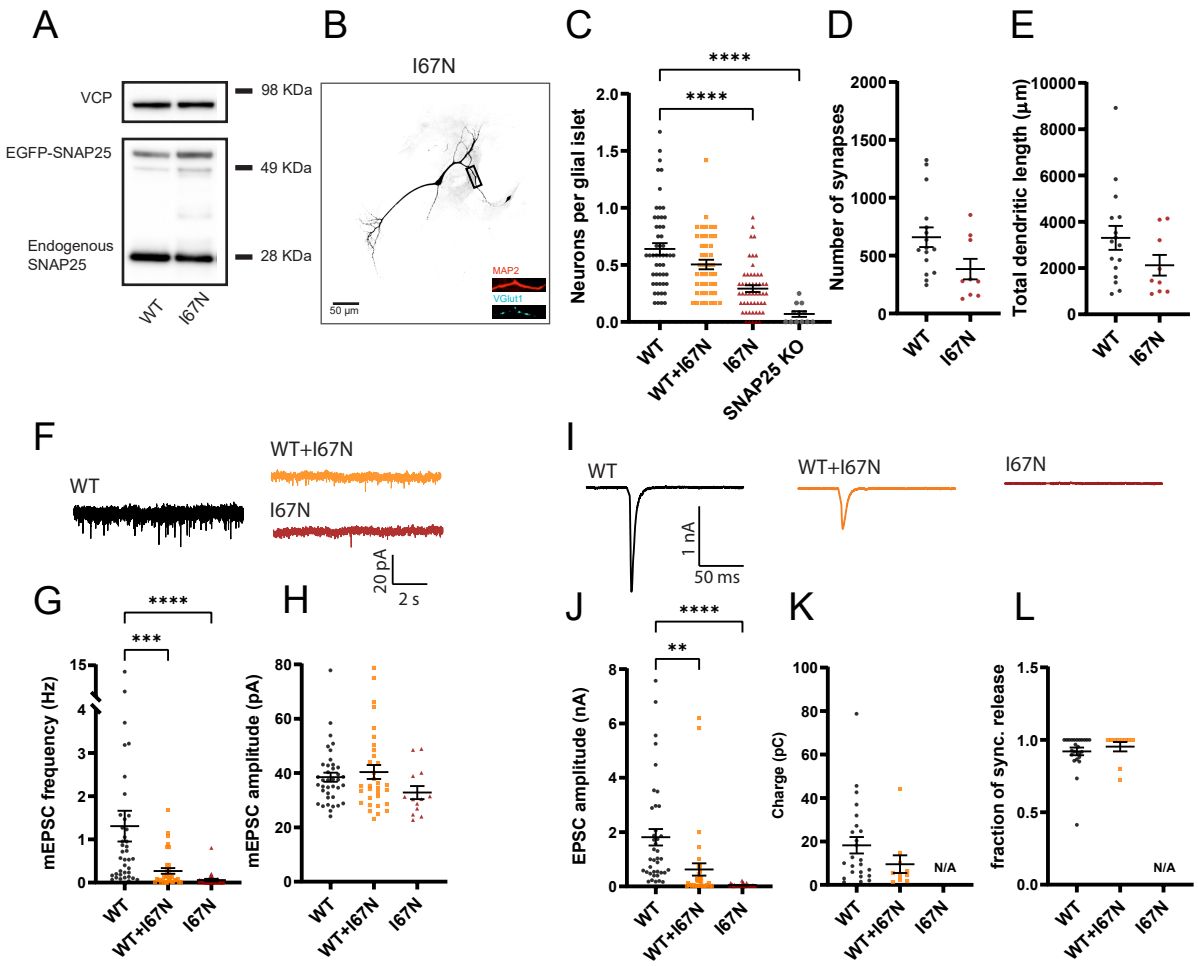

Kádková et al., Fig. 10

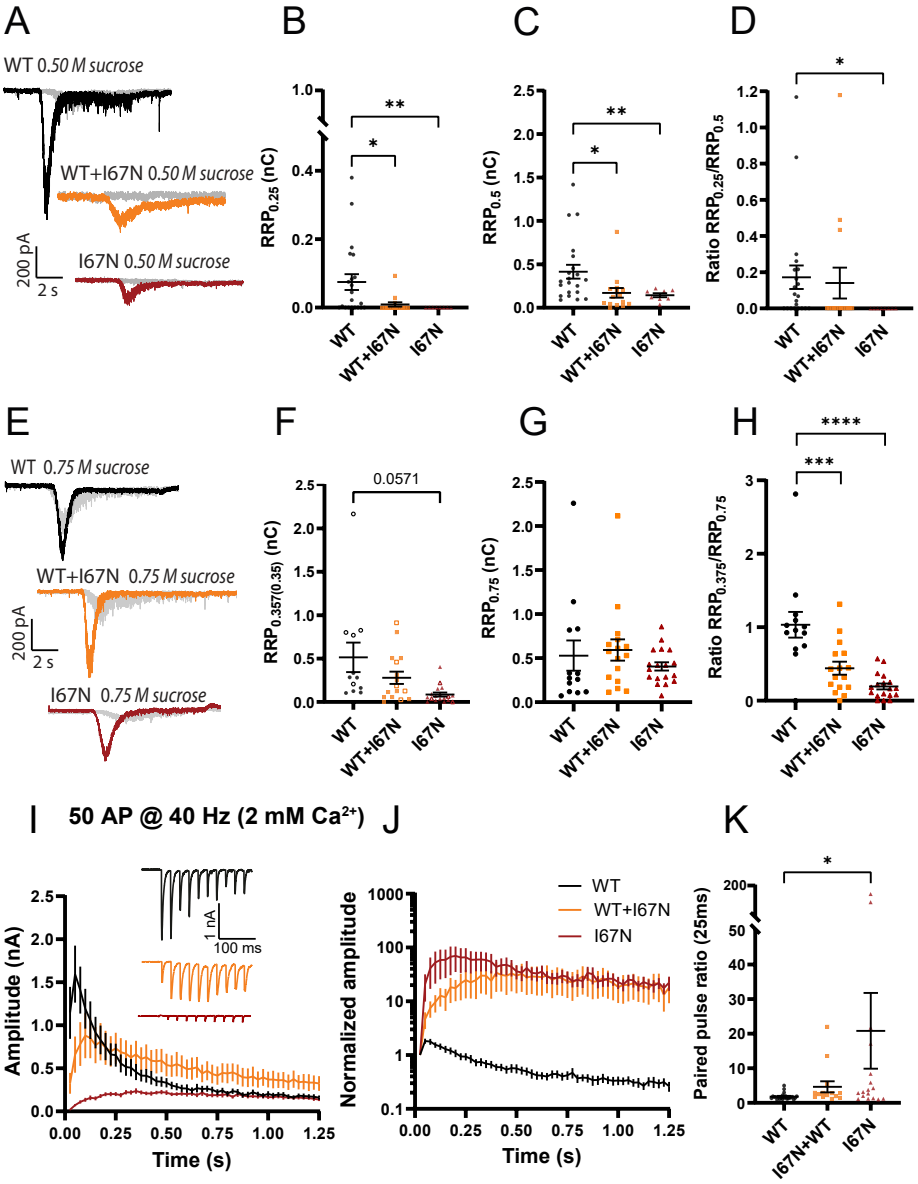

Kádková et al., Fig. 11

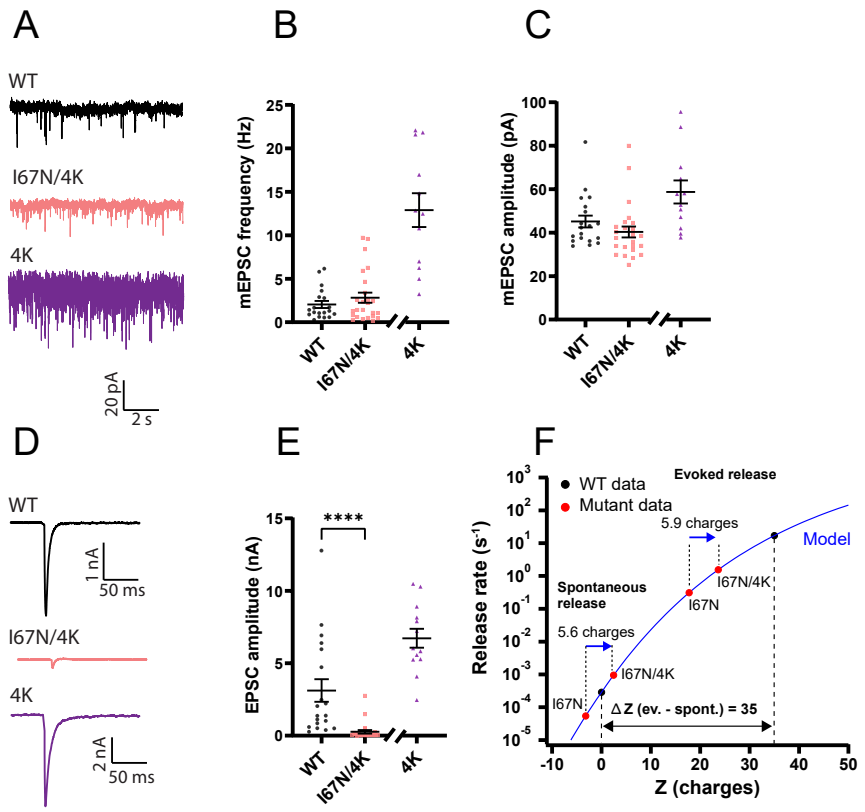

Kádková et al., Fig. 12

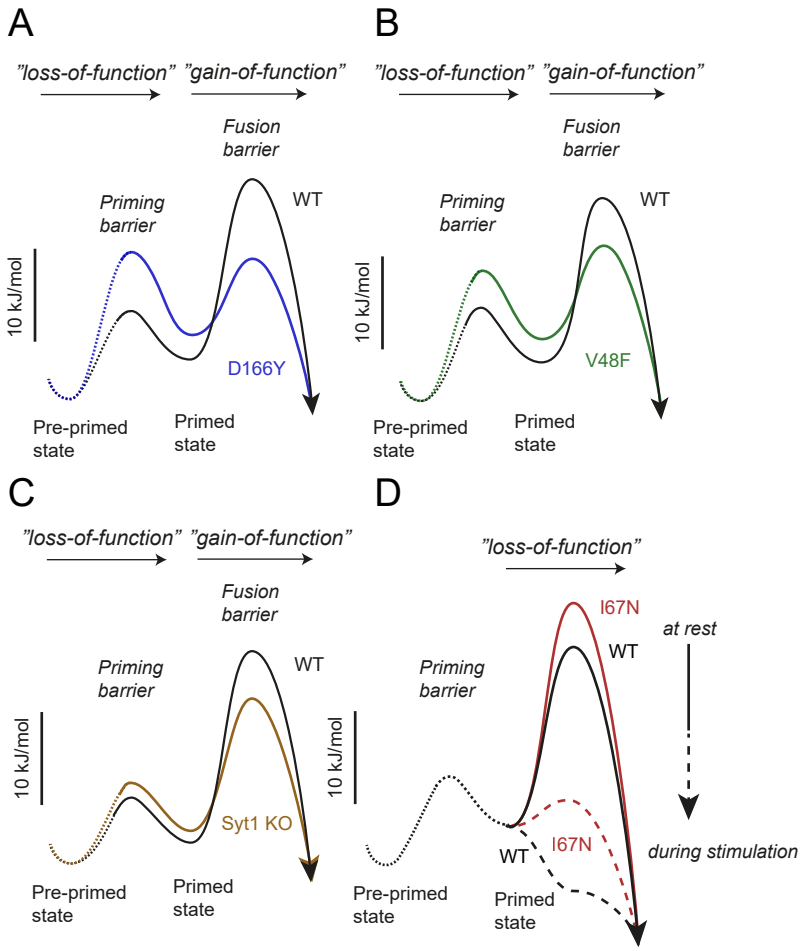

Kádková et al., Fig. 13

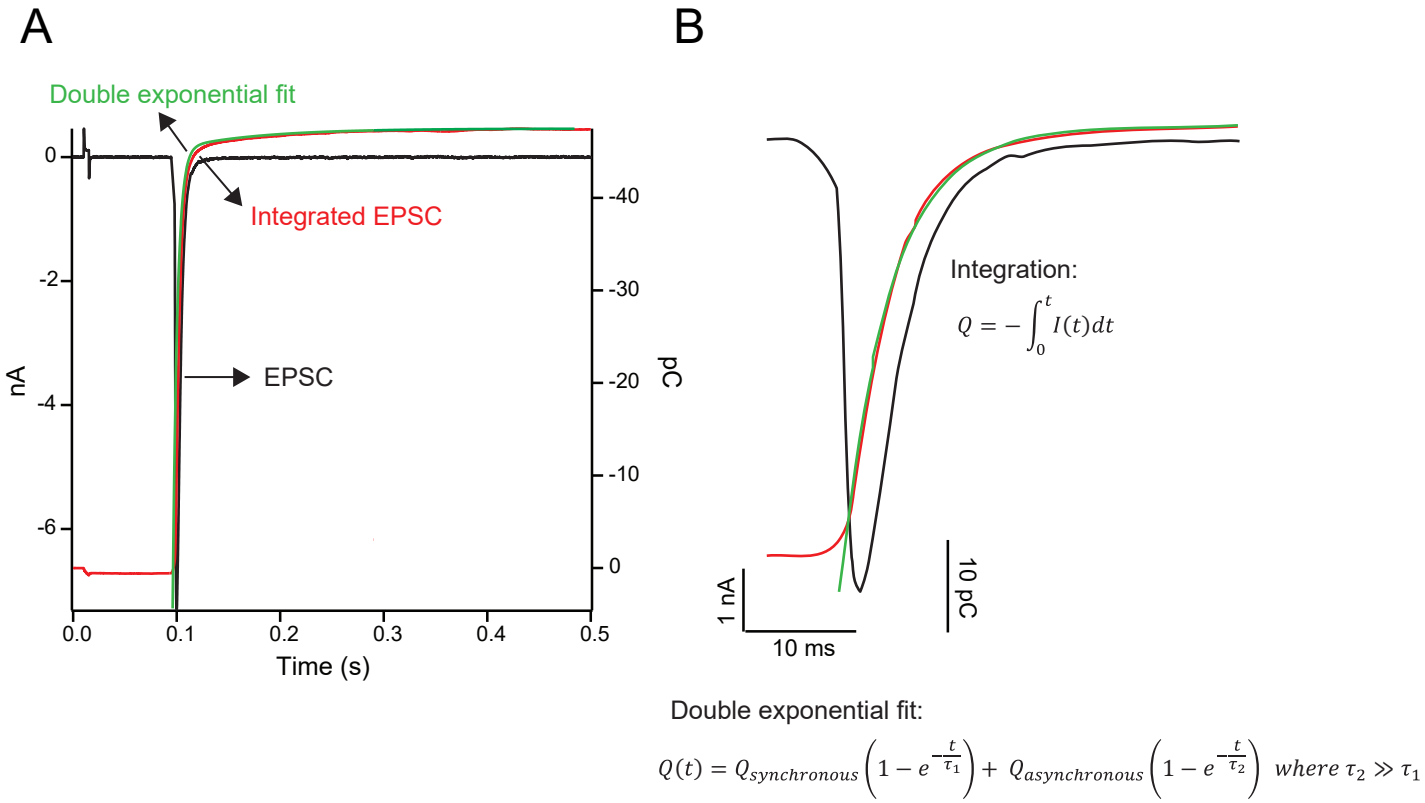

Kádková et al., Fig. 4 - Figure supplement 1

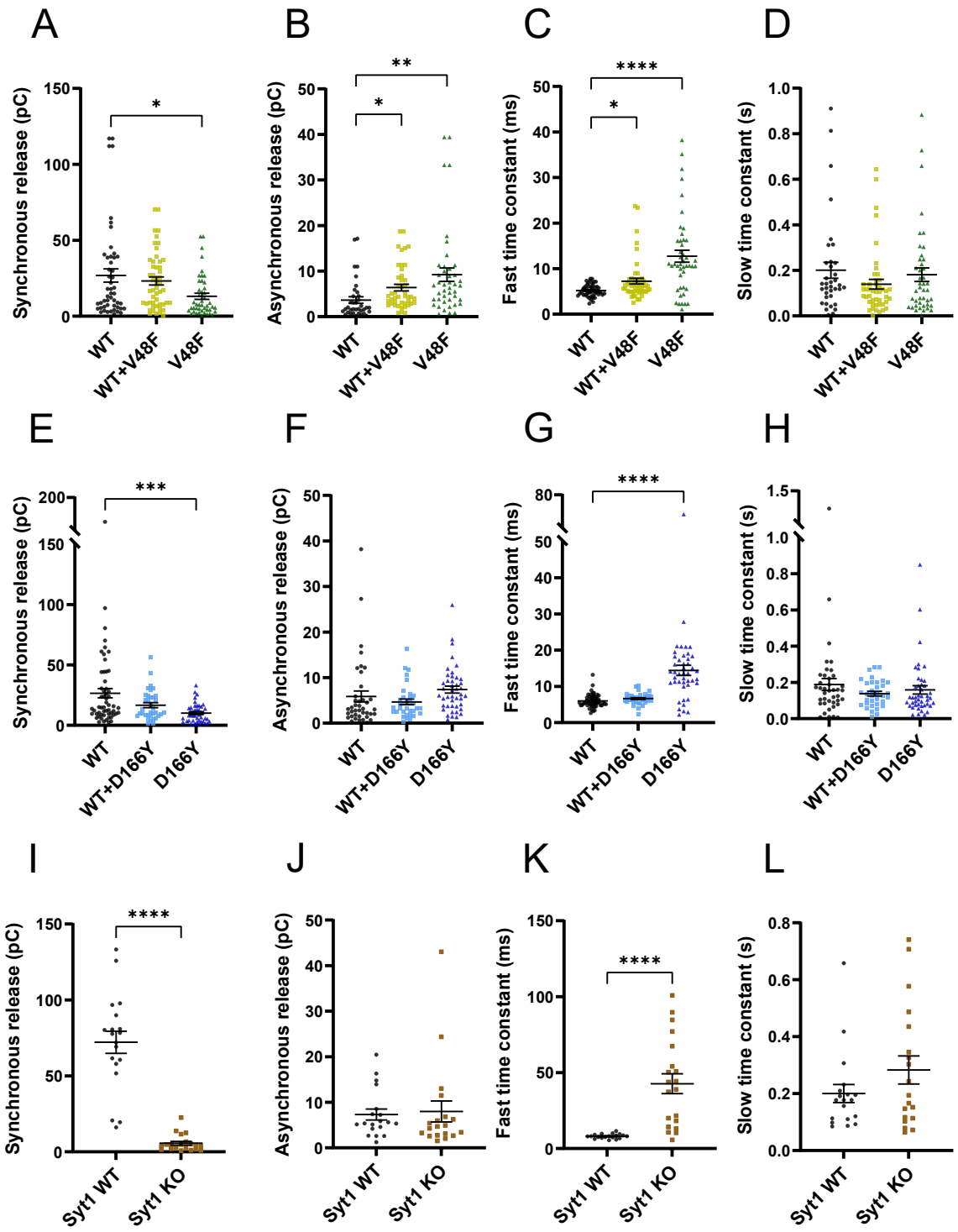

Kádková et al., Fig. 4 - Figure supplement 2

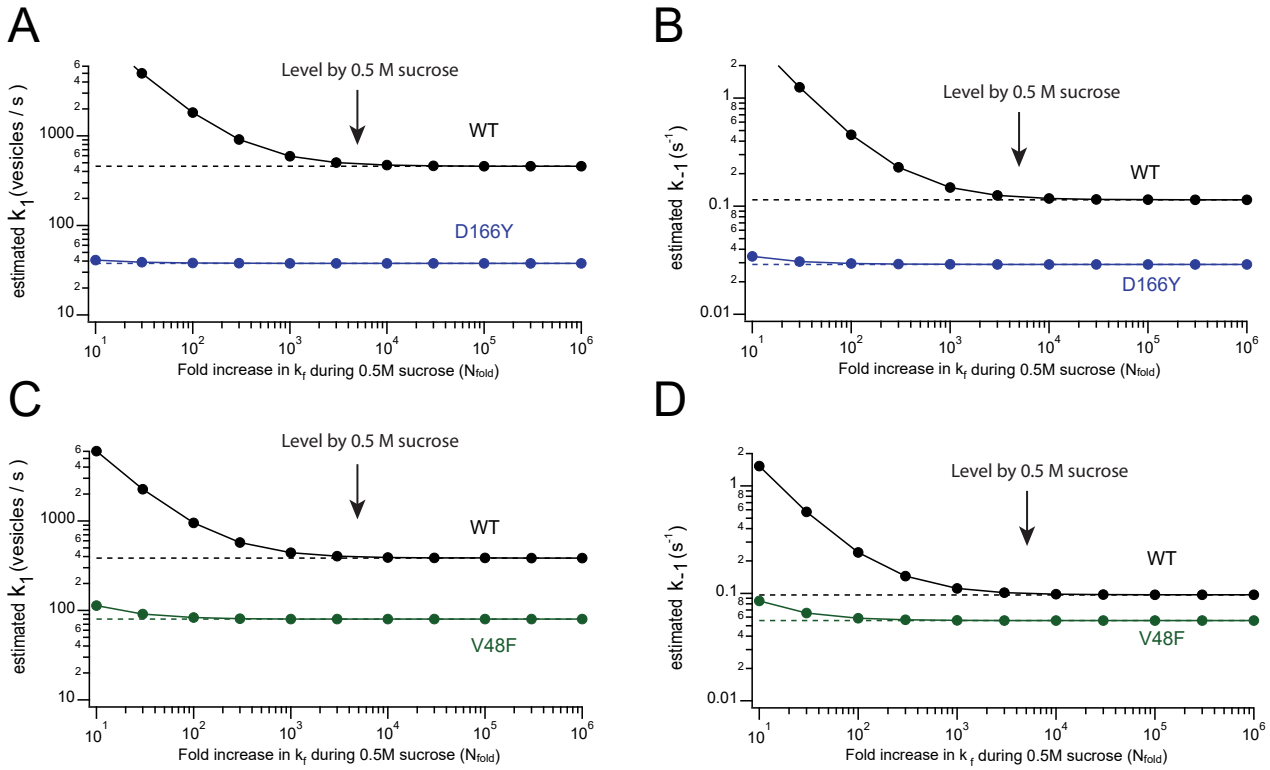

Kádková et al., Fig. 6 - Figure supplement 1

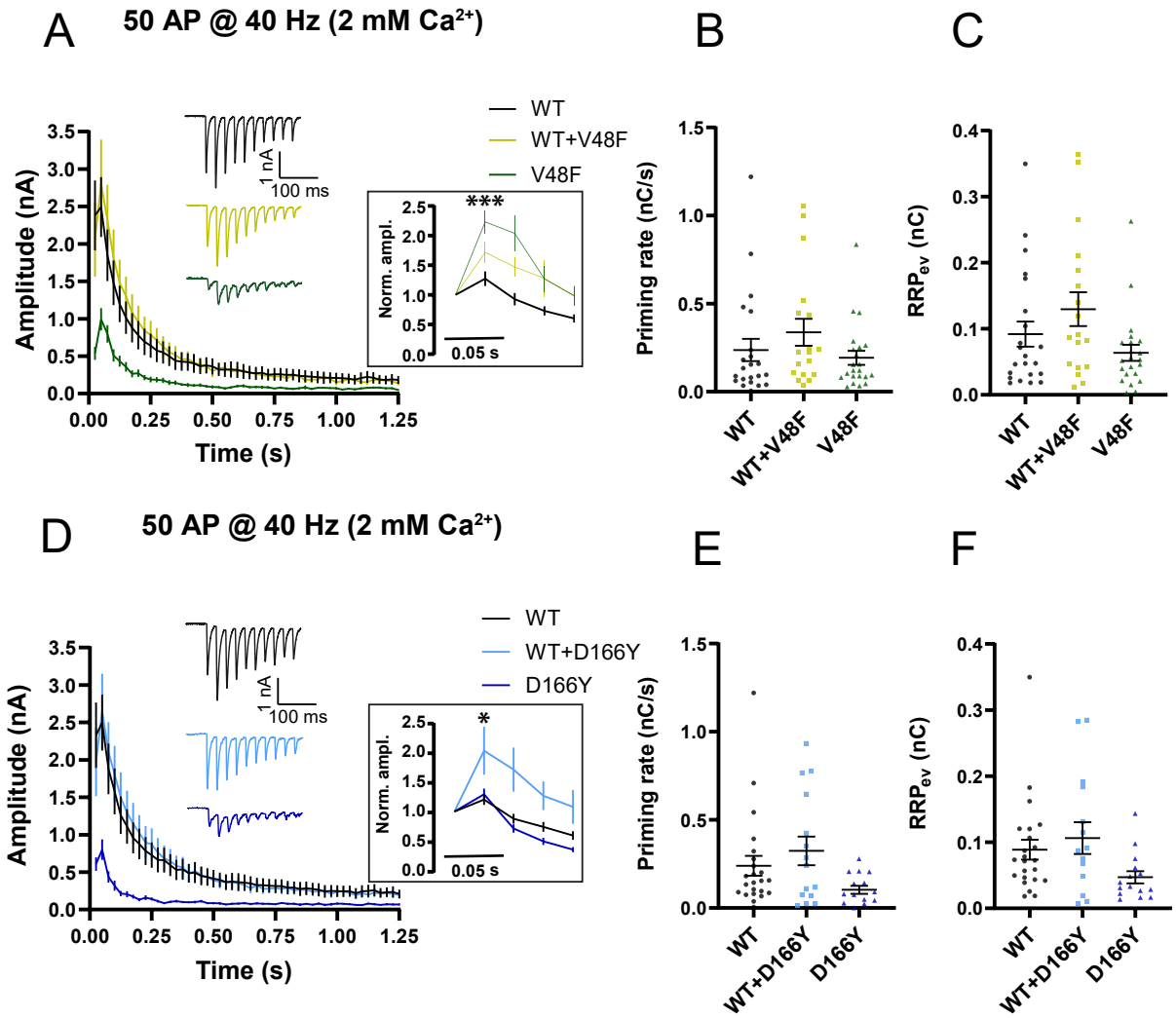

Kádková et al., Fig. 7 - Figure supplement 1

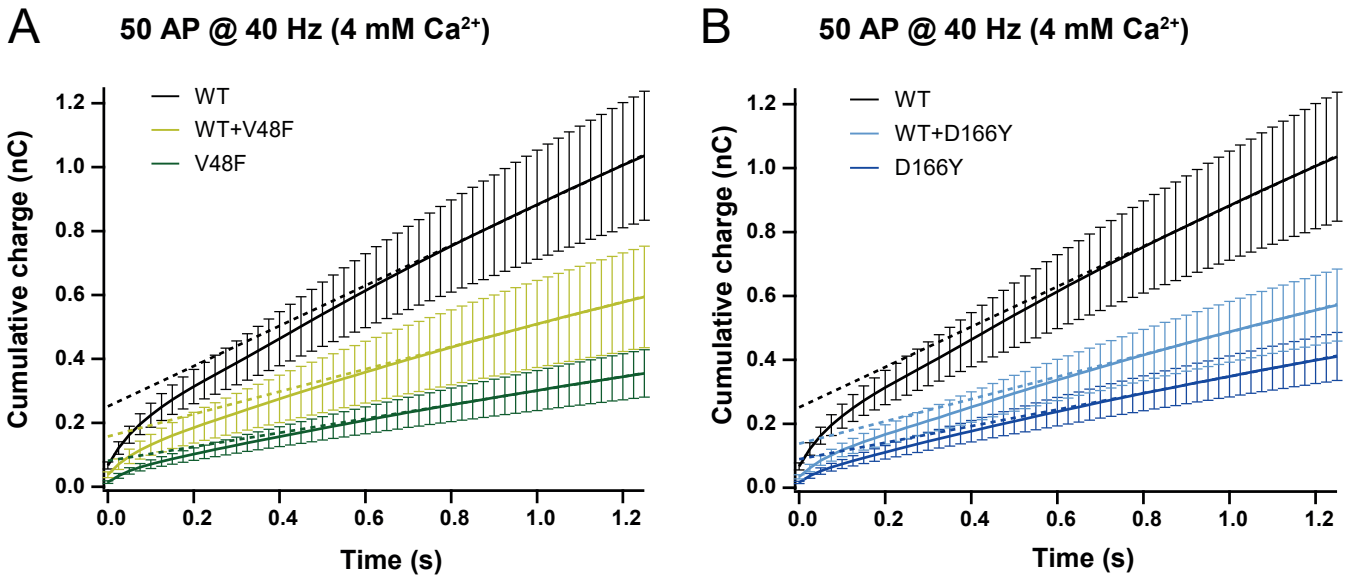

Kádková et al., Fig. 7 - Figure supplement 2

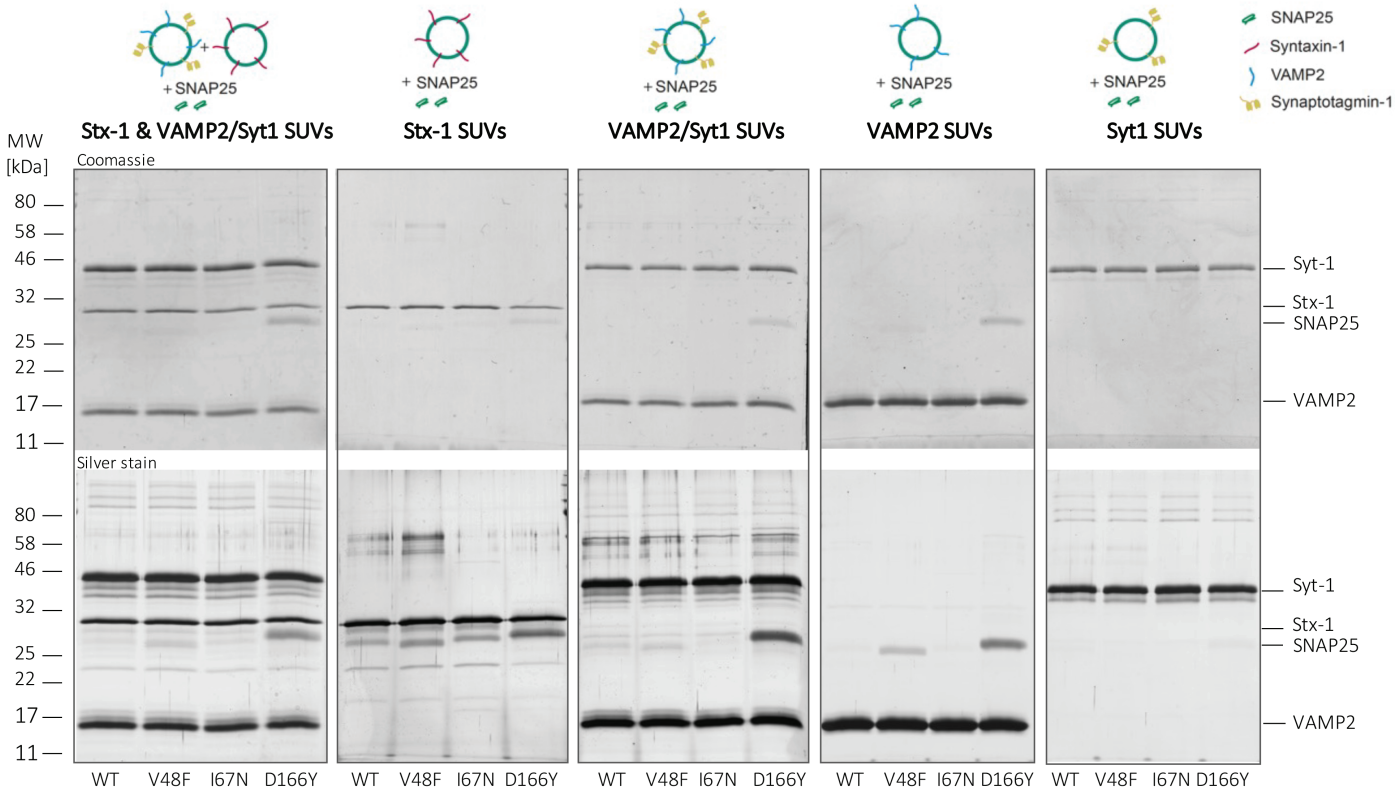

Kádková et al., Fig. 9 - Figure supplement 1

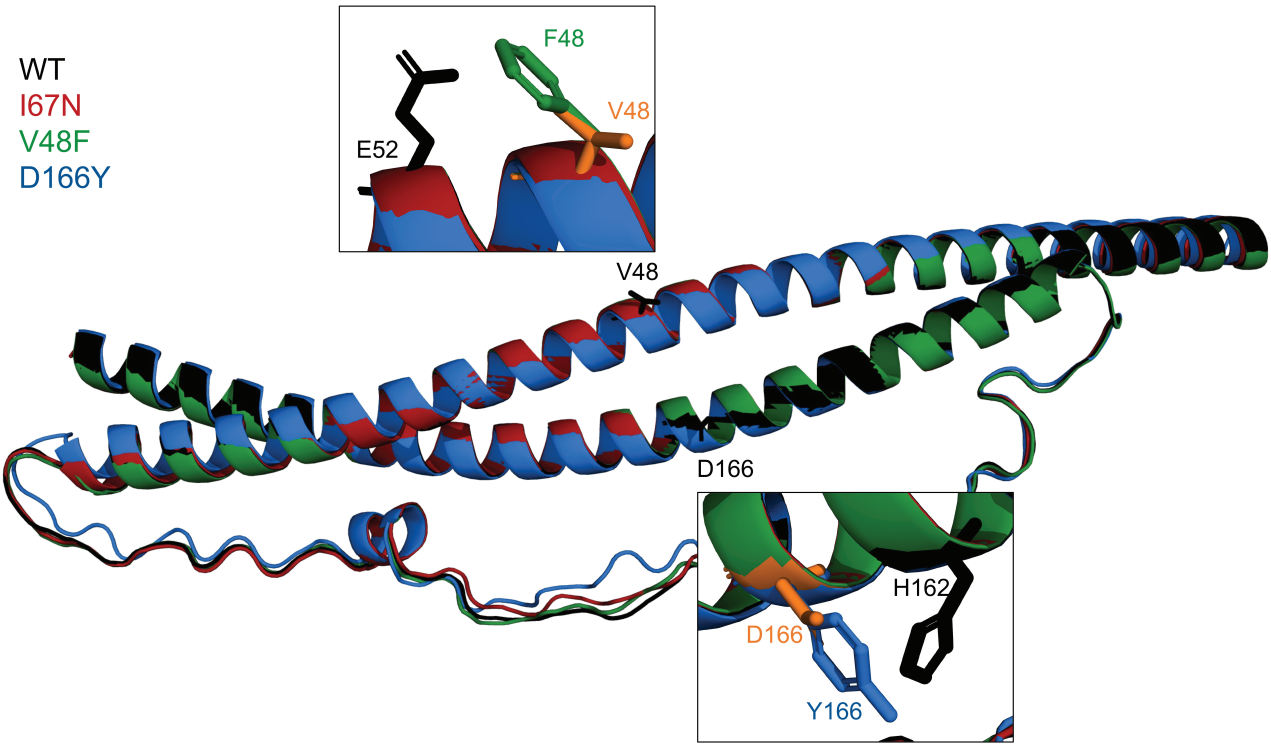

Kádková et al., Fig. 9 - Figure supplement 2